



Simulations of Turbulent Momentum and Scalar Transport in Confined Swirling Coaxial Jets

Tsan-Hsing Shih
Ohio Aerospace Institute, Brook Park, Ohio

Nan-Suey Liu
Glenn Research Center, Cleveland, Ohio

NASA STI Program . . . in Profile

Since its founding, NASA has been dedicated to the advancement of aeronautics and space science. The NASA Scientific and Technical Information (STI) program plays a key part in helping NASA maintain this important role.

The NASA STI Program operates under the auspices of the Agency Chief Information Officer. It collects, organizes, provides for archiving, and disseminates NASA's STI. The NASA STI program provides access to the NASA Aeronautics and Space Database and its public interface, the NASA Technical Reports Server, thus providing one of the largest collections of aeronautical and space science STI in the world. Results are published in both non-NASA channels and by NASA in the NASA STI Report Series, which includes the following report types:

- **TECHNICAL PUBLICATION.** Reports of completed research or a major significant phase of research that present the results of NASA programs and include extensive data or theoretical analysis. Includes compilations of significant scientific and technical data and information deemed to be of continuing reference value. NASA counterpart of peer-reviewed formal professional papers but has less stringent limitations on manuscript length and extent of graphic presentations.
- **TECHNICAL MEMORANDUM.** Scientific and technical findings that are preliminary or of specialized interest, e.g., quick release reports, working papers, and bibliographies that contain minimal annotation. Does not contain extensive analysis.
- **CONTRACTOR REPORT.** Scientific and technical findings by NASA-sponsored contractors and grantees.

- **CONFERENCE PUBLICATION.** Collected papers from scientific and technical conferences, symposia, seminars, or other meetings sponsored or cosponsored by NASA.
- **SPECIAL PUBLICATION.** Scientific, technical, or historical information from NASA programs, projects, and missions, often concerned with subjects having substantial public interest.
- **TECHNICAL TRANSLATION.** English-language translations of foreign scientific and technical material pertinent to NASA's mission.

Specialized services also include creating custom thesauri, building customized databases, organizing and publishing research results.

For more information about the NASA STI program, see the following:

- Access the NASA STI program home page at <http://www.sti.nasa.gov>
- E-mail your question to help@sti.nasa.gov
- Fax your question to the NASA STI Information Desk at 443-757-5803
- Phone the NASA STI Information Desk at 443-757-5802
- Write to:
STI Information Desk
NASA Center for AeroSpace Information
7115 Standard Drive
Hanover, MD 21076-1320

NASA/TM—2014-218134



Simulations of Turbulent Momentum and Scalar Transport in Confined Swirling Coaxial Jets

Tsan-Hsing Shih
Ohio Aerospace Institute, Brook Park, Ohio

Nan-Suey Liu
Glenn Research Center, Cleveland, Ohio

National Aeronautics and
Space Administration

Glenn Research Center
Cleveland, Ohio 44135

August 2014

Acknowledgments

This work is supported by the NASA Fundamental Aeronautics Program. Authors would also like to thank Drs. Jeff Moder and Thomas Wey for providing the information and useful discussion on the water jet simulation using NCC.

This report is a formal draft or working paper, intended to solicit comments and ideas from a technical peer group.

This report contains preliminary findings, subject to revision as analysis proceeds.

Trade names and trademarks are used in this report for identification only. Their usage does not constitute an official endorsement, either expressed or implied, by the National Aeronautics and Space Administration.

This work was sponsored by the Fundamental Aeronautics Program at the NASA Glenn Research Center.

Level of Review: This material has been technically reviewed by technical management.

Available from

NASA Center for Aerospace Information
7115 Standard Drive
Hanover, MD 21076-1320

National Technical Information Service
5301 Shawnee Road
Alexandria, VA 22312

Available electronically at <http://www.sti.nasa.gov>

Simulations of Turbulent Momentum and Scalar Transport in Confined Swirling Coaxial Jets

Tsan-Hsing Shih
Ohio Aerospace Institute
Brook Park, Ohio 44142

Nan-Suey Liu
National Aeronautics and Space Administration
Glenn Research Center
Cleveland, Ohio 44135

Abstract

This paper presents the numerical simulations of confined three dimensional coaxial water jets. The objectives are to validate the newly proposed nonlinear turbulence models of momentum and scalar transport, and to evaluate the newly introduced scalar APDF and DWDFD equation along with its Eulerian implementation in the National Combustion Code (NCC). Simulations conducted include the steady RANS, the unsteady RANS (URANS), and the time-filtered Navier-Stokes (TFNS) with and without invoking the APDF or DWDFD equation. When the APDF or DWDFD equation is invoked, the simulations are of a hybrid nature, i.e., the transport equations of energy and species are replaced by the APDF or DWDFD equation. Results of simulations are compared with the available experimental data. Some positive impacts of the nonlinear turbulence models and the Eulerian scalar APDF and DWDFD approach are observed.

1.0 Introduction

In this study we have focused on two subjects. The first one is to validate the newly proposed nonlinear models of turbulent momentum and scalar transport implemented in the NCC code (Ref. 1) using the experimental data from confined swirling coaxial water jets (Ref. 2), and pay special attention to the relative performance of the nonlinear scalar flux model vs. the linear scalar flux model. The second one is to validate the newly introduced scalar APDF (Ref. 3) and DWDFD (Ref. 4) equations and their Eulerian implementations in the NCC code using the same experimental data.

Both validations have been carried out with three types of numerical simulation approaches. The first two approaches are the steady RANS and the unsteady RANS (URANS). The third one is the time filtered Navier-Stokes (TFNS (Refs. 5 and 6) approach.

The experimental study provided flow structures that are resembling those often existing in a gas turbine combustor, for example, center swirling recirculation near the front of combustor, massive swirled separations at the front corners, strong swirling flow extended all the way to the exit of combustor, and significant changes of concentration in the radial direction at the front of combustor, etc. Detailed experimental data on the velocity and scalar concentration distributions is available for validating the turbulence models and evaluating the numerical simulation approaches. Since water was used in the experiment but NCC solves the compressible Navier-Stokes equations supplemented by the equation of state for ideal gas, the water flow experiment was converted to its corresponding air flow simulation according to the Reynolds number similarity rule under the condition of low speed. The results of air flow simulations were then rescaled back to their water flow counterparts and compared with the experimental data.

The turbulence models for momentum and scalar transport validated in the current simulations are listed in Section 2.1. The APDF and DWDFD equation invoked in the hybrid approach of RANS/APDF, URANS/APDF and TFNS/DWDFD simulations are listed in Section 2.2.

The results of validations of the turbulence models are presented in Sections 3.1, 3.2 and 3.3. The results obtained from the linear scalar flux model and those from the nonlinear scalar flux model in all three types of simulations (RANS, URANS and TFNS) are compared with the available experimental data. The results obtained by invoking the APDF and DWDFD equation are presented in a similar way in Sections 3.4, 3.5 and 3.6. These simulations are of hybrid nature, i.e., the velocity field is solved by the continuity and momentum equations, but the transport equations of energy and species are replaced by the equation of APDF or DWDFD, and the APDF or DWDFD equation is solved by an Eulerian Monte Carlo particle method (Ref. 7). Finally, a brief summary is given in the conclusion.

In addition, an Appendix is presented to compare the different performance of using a standard $k - \varepsilon$ eddy viscosity linear stress model vs. using the present $k - \varepsilon$ nonlinear stress model in the RANS simulations under the exact same conditions. This comparison along with the experimental data clearly demonstrates the improvements made by the turbulent nonlinear stress model.

2.0 Turbulence Models and Scalar PDF Equation

The models for turbulent stress tensor τ_{ij} and scalar flux vector Θ_i , as well as the scalar APDF and DWDFD equation employed in the current simulations are listed in this section.

2.1 Linear Model Versus Nonlinear Model

2.1.1 Linear Models of Turbulent Stresses and Scalar Fluxes

Based on the Boussinesq approximation of the linear relationship between the turbulent stress and the strain rate of flow field, the linear model of turbulent stress is formulated as

$$\tau_{ij} - \frac{1}{3} \delta_{ij} \tau_{kk} = -2 f C_\mu \bar{\rho} \frac{k^2}{\varepsilon} (\tilde{S}_{ij} - \delta_{ij} \tilde{S}_{kk} / 3) \quad (2.1)$$

Similarly, the linear model of turbulent scalar flux is formulated as

$$\Theta_i = -g_T \frac{\partial \bar{\rho} \tilde{\theta}}{\partial x_i} \quad (2.2)$$

2.1.2 Nonlinear Models of Turbulent Stresses and Scalar Fluxes

A general constitutive relationship between the turbulent stresses τ_{ij} and the strain rate of flow field \tilde{S}_{ij} , $\tilde{\Omega}_{ij}$ suggests (Refs. 6 and 8)

$$\begin{aligned} \tau_{ij} - \frac{1}{3} \delta_{ij} \tau_{kk} = & -2 f C_\mu \bar{\rho} \frac{k^2}{\varepsilon} (\tilde{S}_{ij} - \delta_{ij} \tilde{S}_{kk} / 3) \\ & - A_3 f \bar{\rho} \frac{k^3}{\varepsilon^2} (\tilde{S}_{ik} \tilde{\Omega}_{kj} - \tilde{\Omega}_{ik} \tilde{S}_{kj}) \\ & + 2 A_5 f \bar{\rho} \frac{k^4}{\varepsilon^3} \left[\tilde{\Omega}_{ik} \tilde{S}_{kj}^2 - \tilde{S}_{ik}^2 \tilde{\Omega}_{kj} + \tilde{\Omega}_{ik} \tilde{S}_{km} \tilde{\Omega}_{mj} - \tilde{\Omega}_{kl} \tilde{S}_{lm} \tilde{\Omega}_{mk} \delta_{ij} / 3 + II_s (\tilde{S}_{ij} - \delta_{ij} \tilde{S}_{kk} / 3) \right], \end{aligned} \quad (2.3)$$

where, $\tilde{S}_{ij} = (\tilde{U}_{i,j} + \tilde{U}_{j,i}) / 2$, $\tilde{\Omega}_{ij} = (\tilde{U}_{i,j} - \tilde{U}_{j,i}) / 2$, $II_s = (\tilde{S}_{kk} \tilde{S}_{mm} - \tilde{S}_{kl} \tilde{S}_{lk}) / 2$. The model coefficients C_μ , A_3 and A_5 are constrained by the realizability condition and the rapid distortion theory. They are formulated as (see Ref. 9):

$$C_\mu = \frac{1}{4.0 + A_s \frac{k}{\varepsilon} U^*}, \quad A_3 = \frac{\sqrt{1.0 - A_s^2 C_\mu^2 \left(\frac{k}{\varepsilon} S^*\right)^2}}{0.5 + 1.5 \frac{k^2}{\varepsilon^2} \Omega^* S^*}, \quad A_5 = \frac{1.6 C_\mu \bar{\rho} \frac{k^2}{\varepsilon}}{\bar{\rho} \frac{k^4}{\varepsilon^3} \frac{7 S^* S^* + \Omega^* \Omega^*}{4}}, \quad (2.4)$$

in which,

$$A_s = \sqrt{6} \cos \varphi, \quad \varphi = \frac{1}{3} \arccos(\sqrt{6} W^*), \quad W^* = \frac{S_{ij}^* S_{jk}^* S_{ki}^*}{(S^*)^3}, \quad (2.5)$$

$$U^* = \sqrt{(S^*)^2 + (\Omega^*)^2}, \quad S^* = \sqrt{S_{ij}^* S_{ij}^*}, \quad \Omega^* = \sqrt{\tilde{\Omega}_{ij} \tilde{\Omega}_{ij}}, \quad S_{ij}^* = \tilde{S}_{ij} - \frac{1}{3} \delta_{ij} \tilde{S}_{kk} \quad (2.6)$$

The coefficient f is a function of filtering Resolution Control Parameter (RCP) that is defined as a ratio of the time filter width Δ_T to a global integral time scale of the flow T : $RCP = \Delta_T/T$ and

$$f\left(\frac{\Delta_T}{T}\right) \approx 2\left(\frac{\Delta_T}{T}\right) - \left(\frac{\Delta_T}{T}\right)^2 \quad (2.7)$$

As discussed in Reference 6, RCP may be viewed as a percentage measure of the unresolved subscale turbulent kinetic energy relative to the total turbulent kinetic energy. Therefore, the value of RCP and the coefficient f are always between 0 and 1, and $f = 1.0$ in RANS and URANS simulations, $f < 1.0$ in TFNS simulations.

Similarly, the nonlinear model for scalar fluxes is formulated as (Ref. 10),

$$\Theta_i = -\vartheta_T \frac{\partial \bar{\rho} \tilde{\theta}}{\partial x_i} - \vartheta_T \frac{k}{\varepsilon} (c_1 \tilde{S}_{ij} + c_2 \tilde{\Omega}_{ij}) \frac{\partial \bar{\rho} \tilde{\theta}}{\partial x_j} \quad (2.8)$$

Where ϑ_T denotes the turbulent diffusivity for the corresponding scalar quantity θ . It is often approximated by $\vartheta_T = \nu_T / Pr^\theta$, where Pr^θ represents the turbulent Prandtl number or Schmidt number depending on whether the scalar quantity $\tilde{\theta}$ is the internal energy \tilde{e} or the species mass fraction $\tilde{\Phi}_m$. The turbulent eddy viscosity is defined as $\nu_T = f \cdot C_\mu \cdot k^2 / \varepsilon$. The coefficients c_1 and c_2 in the current simulations are set to be $c_1 = c_2 = -0.24$.

2.1.3 Model Equations of Turbulent Kinetic Energy and Its Dissipation Rate

The (subscale or total) turbulent kinetic energy and its dissipation rate k , ε will be determined from the following model equations:

$$\frac{\partial}{\partial t} \bar{\rho} k + \frac{\partial}{\partial x_i} \bar{\rho} \tilde{u}_i k = \frac{\partial}{\partial x_i} \left[(\mu + \mu_T) \frac{\partial}{\partial x_i} k \right] - \tau_{ij} \tilde{S}_{ij} - \bar{\rho} \varepsilon \quad (2.9)$$

$$\frac{\partial}{\partial t} \bar{\rho} \varepsilon + \frac{\partial}{\partial x_i} \bar{\rho} \tilde{u}_i \varepsilon = \frac{\partial}{\partial x_i} \left[(\mu + \mu_T) \frac{\partial}{\partial x_i} \varepsilon \right] - C_{\varepsilon 1} \tau_{ij} \tilde{S}_{ij} \frac{\varepsilon}{k} - C_{\varepsilon 2} \frac{\bar{\rho} \varepsilon^2}{k} \quad (2.10)$$

where $C_{\varepsilon 1}$ and $C_{\varepsilon 2}$ are model coefficients. We have adopted the commonly used values of $C_{\varepsilon 1} = 1.45$ and $C_{\varepsilon 2} = 1.92$ in the present simulations.

2.2 Scalar APDF and DWDFD Equation

The transport equation for the scalar APDF or DWDFD, $F_{\Phi}(\boldsymbol{\psi}; \mathbf{x}, t)$, can be written as (Refs. 3 and 4)

$$\frac{\partial F_{\Phi}}{\partial t} + \frac{\partial(\tilde{U}_i F_{\Phi})}{\partial x_i} = \left\{ \frac{\partial}{\partial x_i} \left(\left(\Gamma^{(m)} + \Gamma_T^{(m)} \right) \frac{\partial F_{\Phi}}{\partial x_i} \right) \right\} - \frac{\partial}{\partial \psi_k} (F_{\Phi} \cdot S_k(\boldsymbol{\psi})) + f \cdot \frac{\partial}{\partial \psi_k} \left(\psi_k \frac{1}{\tau} F_{\Phi} \right), \quad k = 1, 2, \dots, M + 1 \quad (2.11)$$

where f is defined in Equation (2.7) and

$$\frac{1}{\tau} \approx \sqrt{\tilde{S}_{ij} \tilde{S}_{ij} + \tilde{\Omega}_{ij} \tilde{\Omega}_{ij}}, \quad \tau \geq \sqrt{(\nu + \nu_T) / \varepsilon} \quad (2.12)$$

3.0 Results of Numerical Simulations

Figure 1 shows the computational domain and the unstructured grid (Ref. 11), which consists of 849,189 tetrahedral elements having 152,555 nodes. Based on the Reynolds number similarity, the case of swirling coaxial water jets was scaled to the case of swirling coaxial air jets, so that it is appropriate to use the NCC code to simulate this low Mach number flow. The water dye concentration was represented by the mass fraction of the dyed air. There are two inlet boundaries, one is for the inner tube, at which the velocity, temperature and density were specified: 25.87 m/s, 300 K, and 1.1774 kg/m³; another one is for the annulus, at which radial profile was specified. The annular air passes through eight swirlers resulting in an annular swirling jet dumped into a suddenly expanded chamber and mixed with the inner dyed air jet. Complex flow features exist in the chamber: shear layers, massive separations near the front corner of the chamber and the center recirculation, etc., see Figure 2. At the exit of the chamber, the pressure of 1.0 atm. was specified for RANS and URANS simulations, whereas an unsteady convective boundary condition was specified for TFNS simulations.

The results of numerical simulations will be presented in the following six sections, each one focuses on a different simulation approach, namely, RANS, URANS, TFNS, RANS/APDF, URANS/APDF, and TFNS/DWDFD.

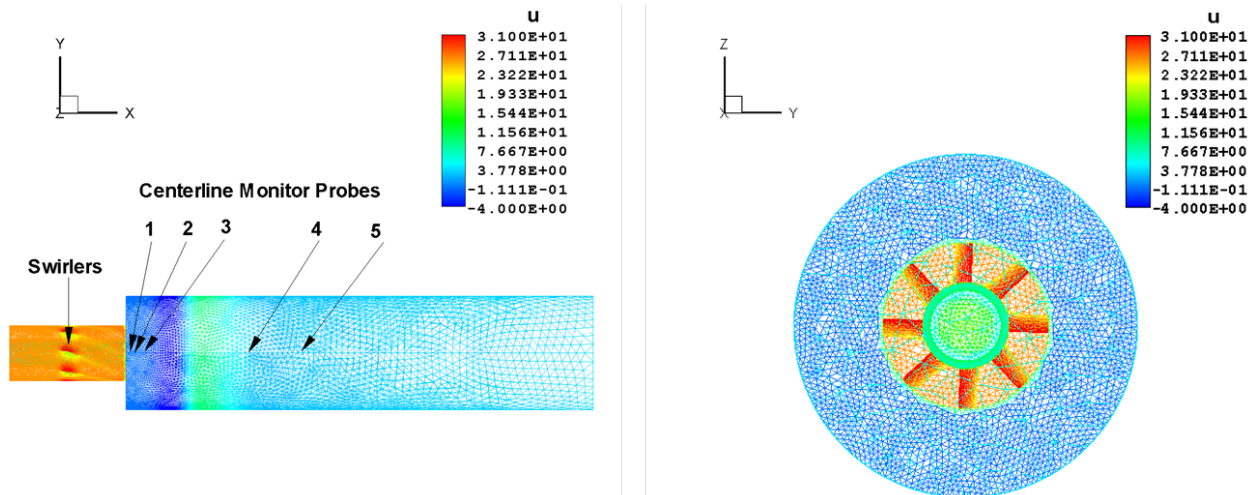


Figure 1.—Computational domain and grid.

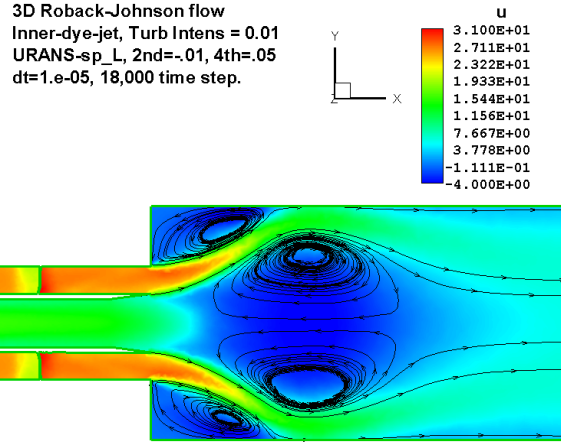


Figure 2.—Flow structures in the center X-Y plane.

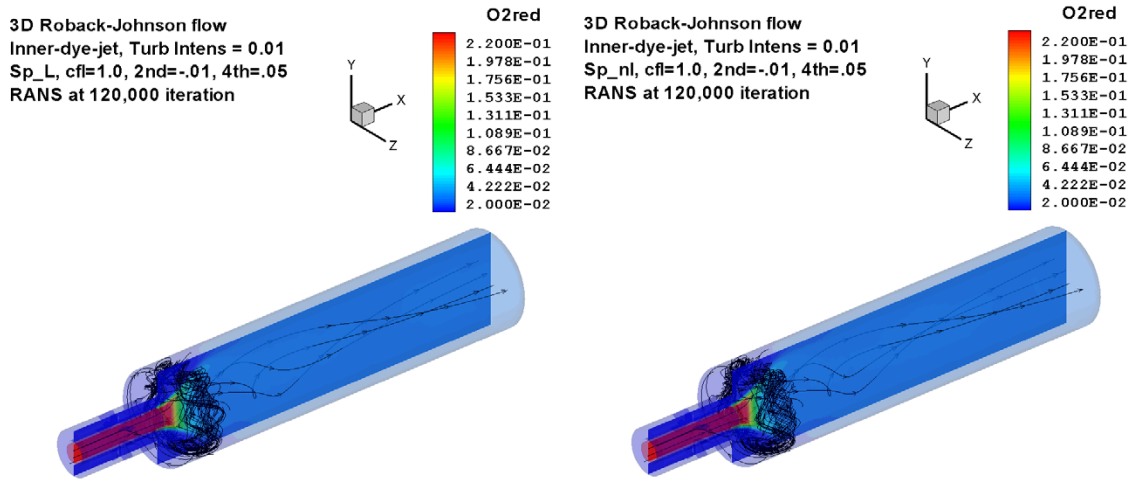


Figure 3.—Global feature of RANS with linear and nonlinear scalar flux models.

In the first three sections, the main interest is in the turbulent scalar flux models, i.e., the performance of nonlinear scalar flux model versus the performance of linear scalar flux model. It is noted here that the turbulent stress model used in the current simulations is always the nonlinear model that has already been validated in the past studies. In this study we use the experimental data of dye concentration to validate the newly proposed nonlinear scalar flux model.

In the next three sections, the main interest is in the hybrid approach, in which the scalar APDF or DWDFD equation (Refs. 3 and 4) is invoked to replace the transport equations of energy and species, and an Eulerian solver for the APDF or DWDFD equation is employed. The numerical results from the hybrid RANS/APDF, URANS/APDF and TFNS/DWDFD approaches are compared with the experimental data.

3.1 Results of RANS Simulations With Linear and Nonlinear Scalar Flux Models

The parameter setting in NCC for the steady RANS calculations are: $cfl = 1.0$, $mass\text{-}imbalance = 1.0 \times 10^{-3}$, $2nd\text{-}smoothing\text{-}coeff = -0.01$, $4th\text{-}smoothing\text{-}coeff = 0.05$. The global feature of the simulations is shown in Figure 3, the left one is RANS with the linear scalar flux model, the right one is RANS with the nonlinear scalar flux model. More detailed results and comparisons will follow.

3.1.1 Evolutions of Velocity Components at Probes Along the Centerline

Figure 4 shows the iteration history of velocity components at probes 3 and 5. They indicate that the computed flow field is not perfectly steady (see the axial velocity u), especially near the front part of the chamber.

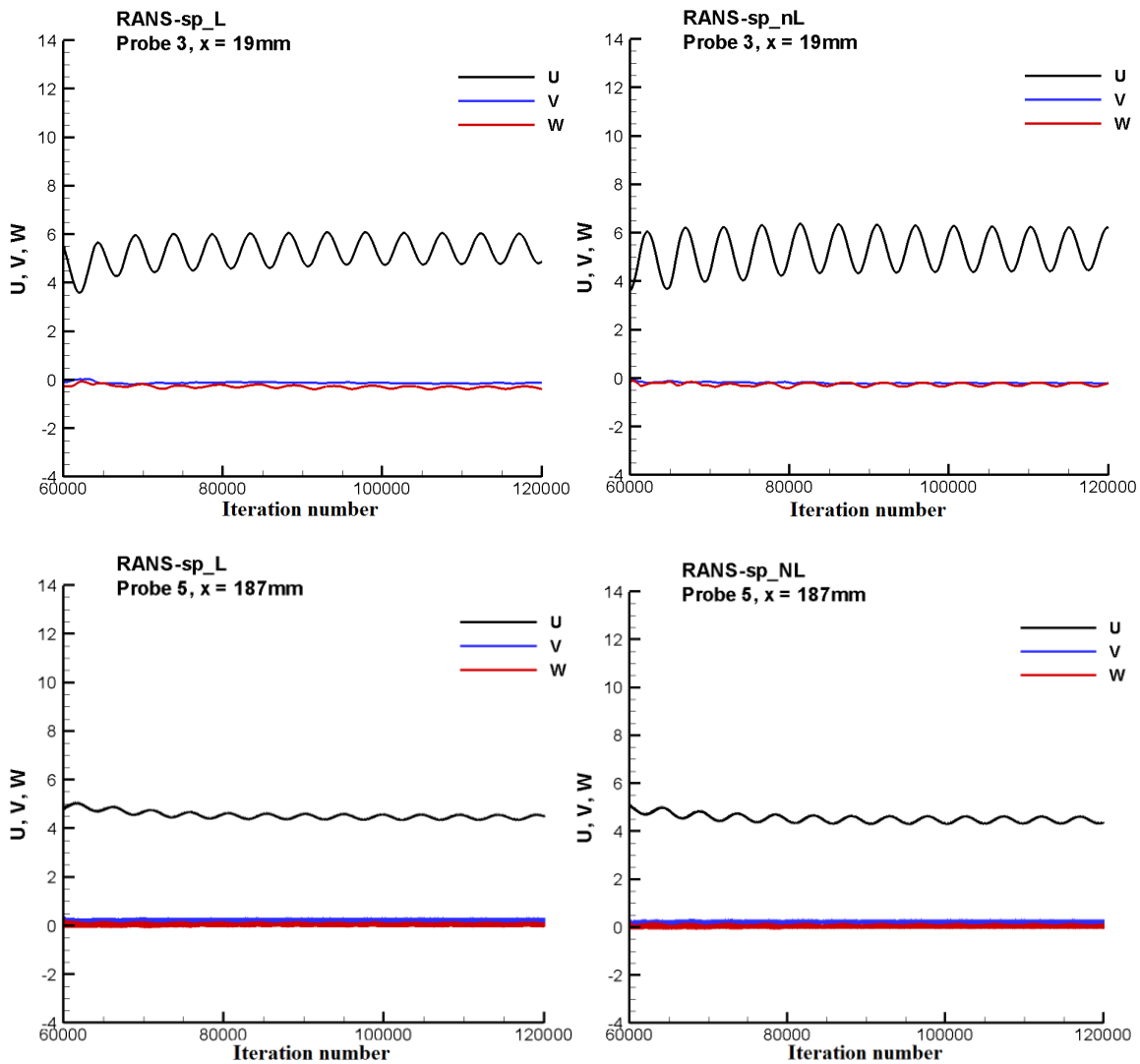


Figure 4.—Iteration history of the computed velocity components at probes 3 and 5.

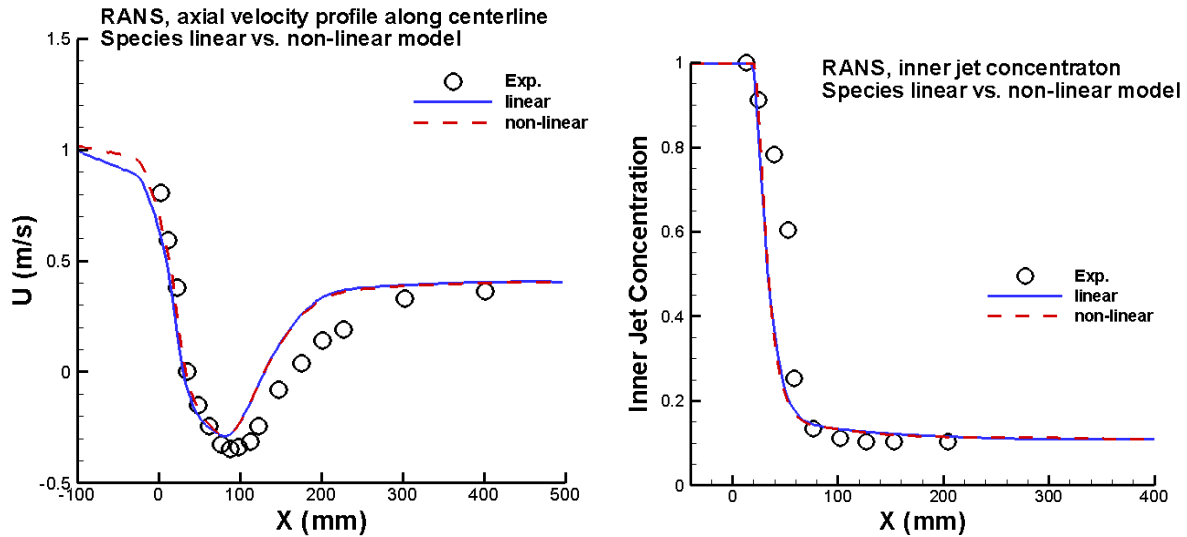


Figure 5.—Centerline distributions of axial velocity and concentration.

3.1.2 Centerline Distribution of the Axial Velocity and the Dye Concentration

Figure 5 indicates that results from both simulations (using linear as well as nonlinear turbulent scalar flux model, respectively) are consistent with the experimental data, and there are no appreciable differences between the results from the two models.

3.1.3 Radial Distribution of the Concentration at Downstream Locations

The radial profiles of dye concentration at five downstream locations ($x = 13, 25, 51, 102, 203$ mm) are shown in Figure 6. Again, results from both simulations match the experimental data reasonably well, except for the location at $x = 51$ mm. The differences between the results from the two models are negligible.

3.1.4 Radial Distribution of Mean Velocity Components U, V, W at Downstream Locations

The radial profiles of axial velocity U , radial velocity V and azimuthal velocity W at seven downstream locations ($x = 5, 25, 51, 102, 152, 203, 406$ mm) are presented in Figure 7, Figure 8 and Figure 9. Results from both simulations match the experimental data quite well, except for the azimuthal velocity W at the further downstream locations $x = 203, 420$ mm, where the computed W are under predicted compared with the experimental data. The differences of results from the two models are negligible.

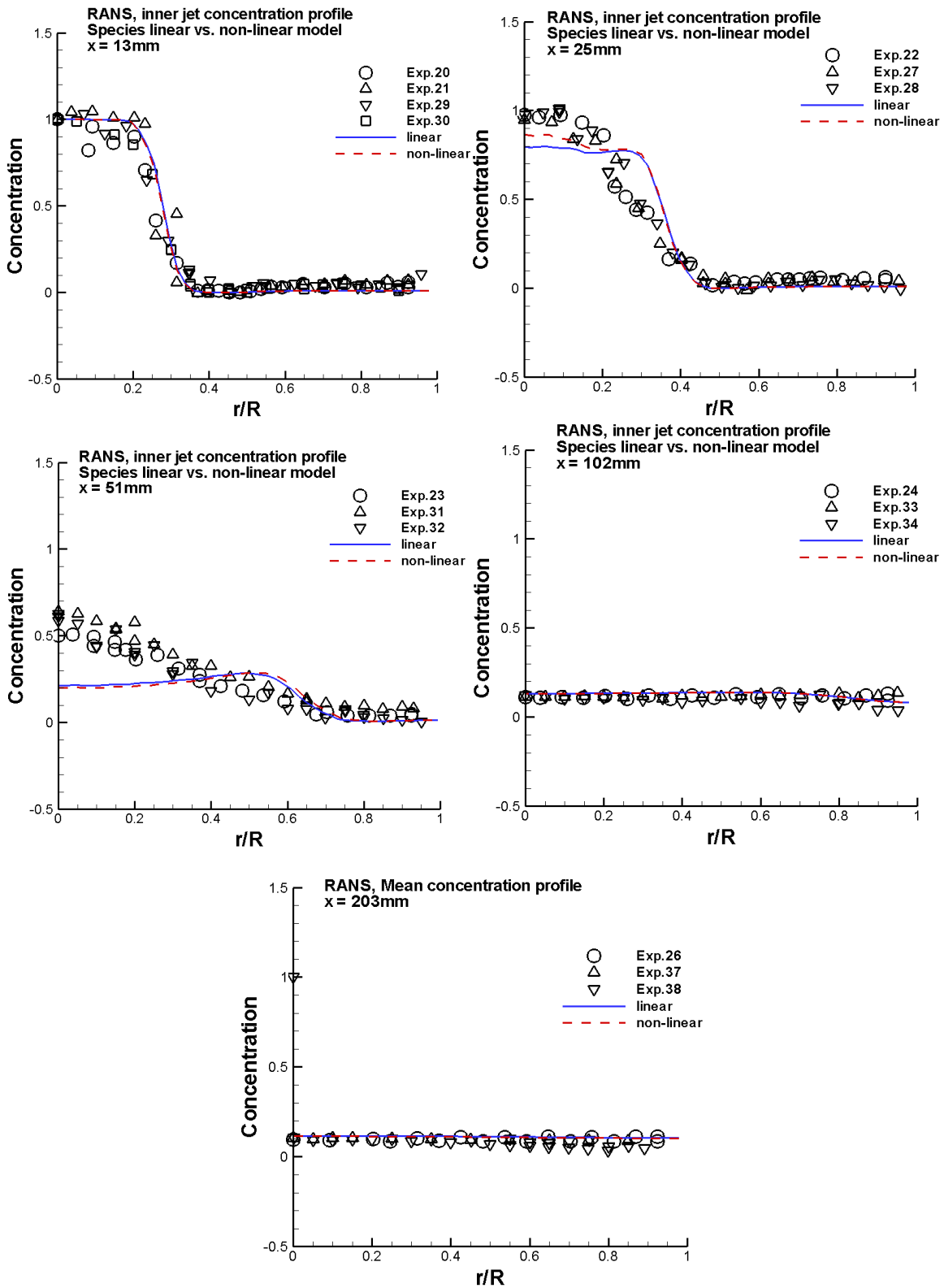


Figure 6.—Radial profiles of mean concentration at downstream locations.

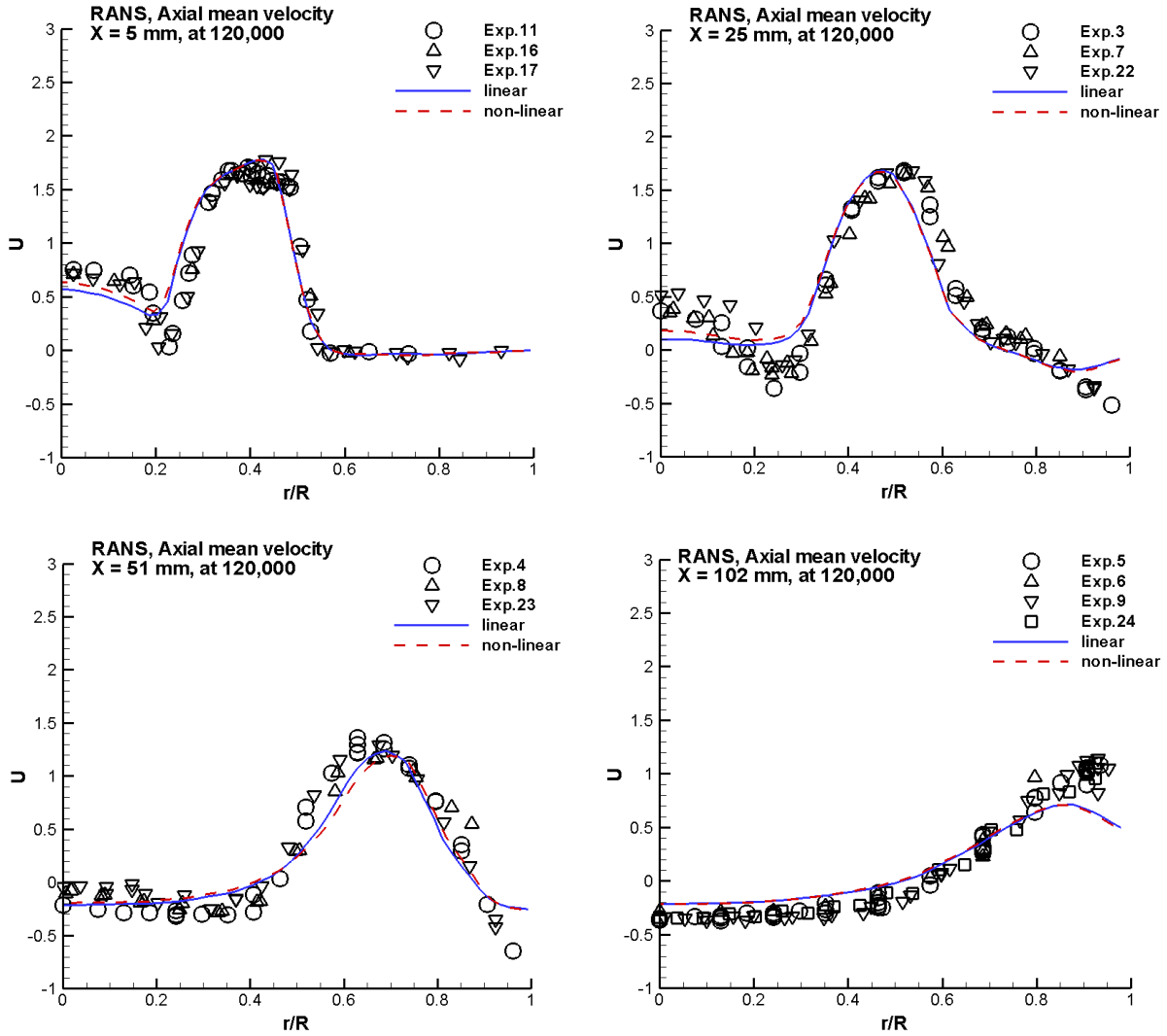


Figure 7.—Radial profiles of axial velocity U at downstream locations.

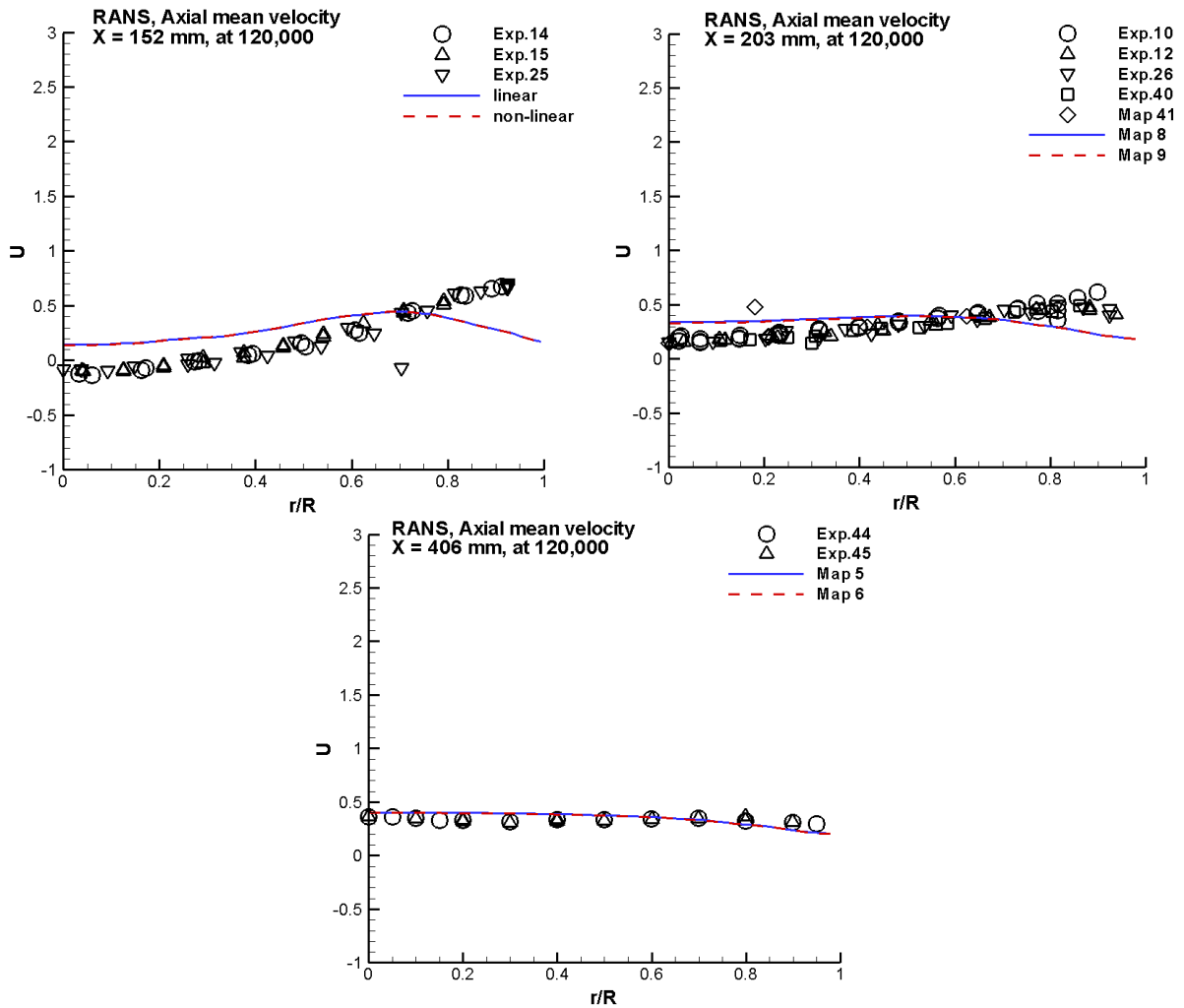


Figure 7.—Concluded.

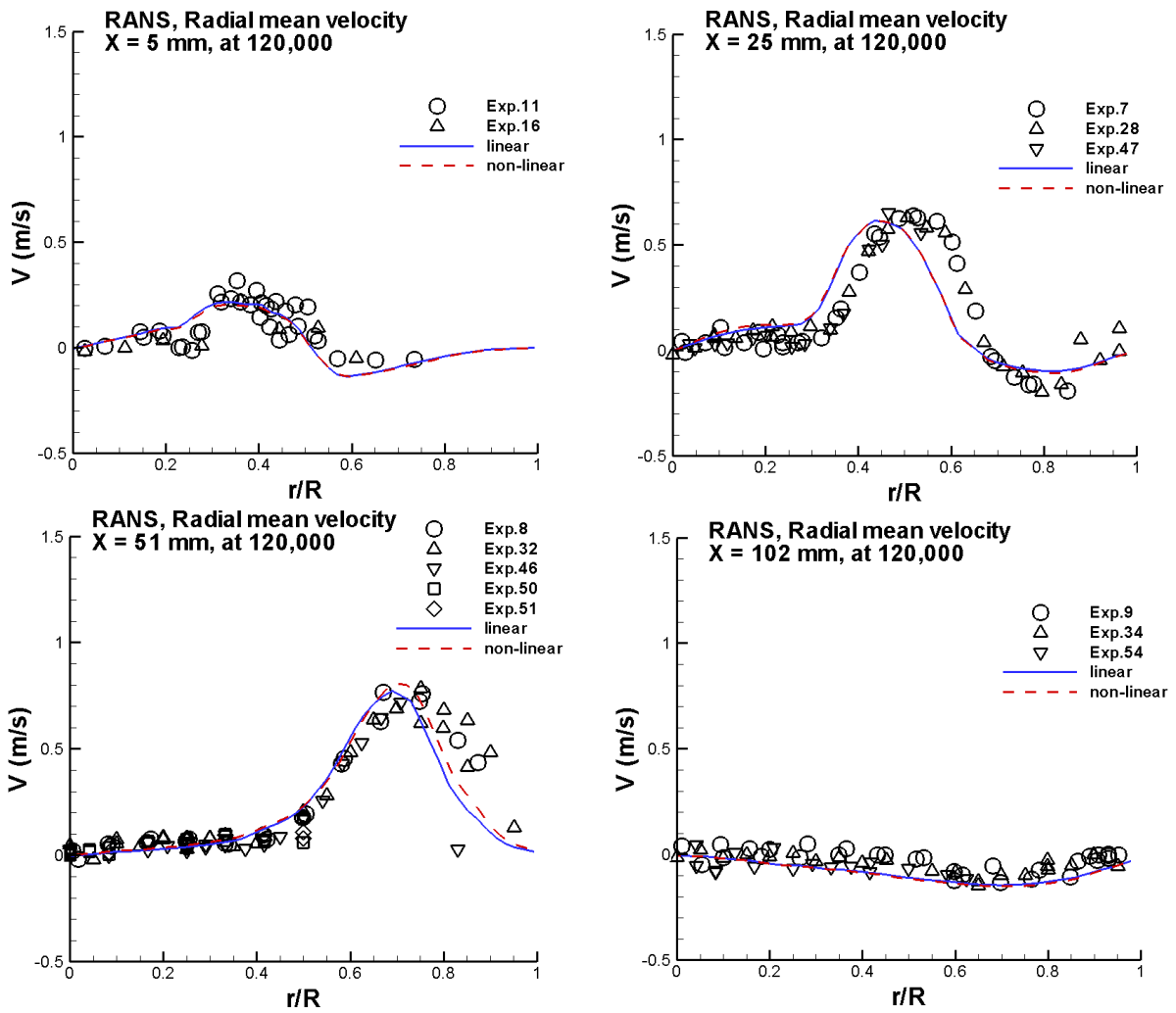


Figure 8.—Radial profiles of radial velocity V at downstream locations.

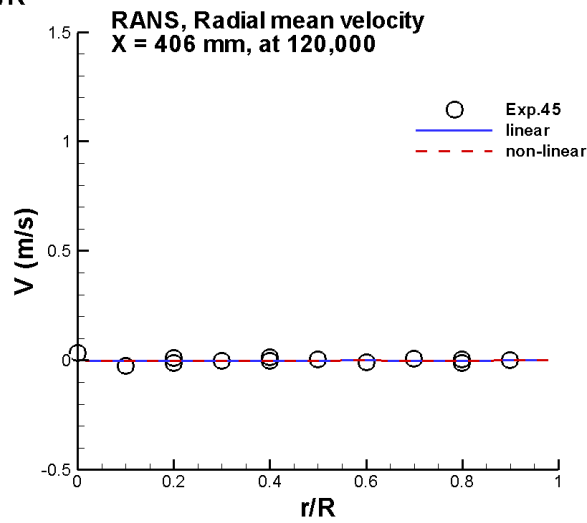
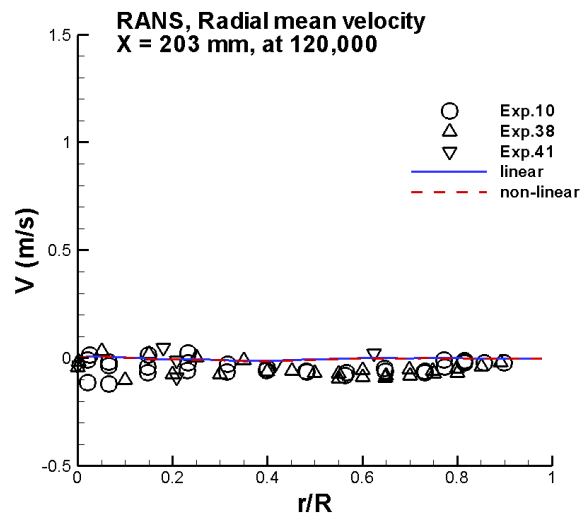
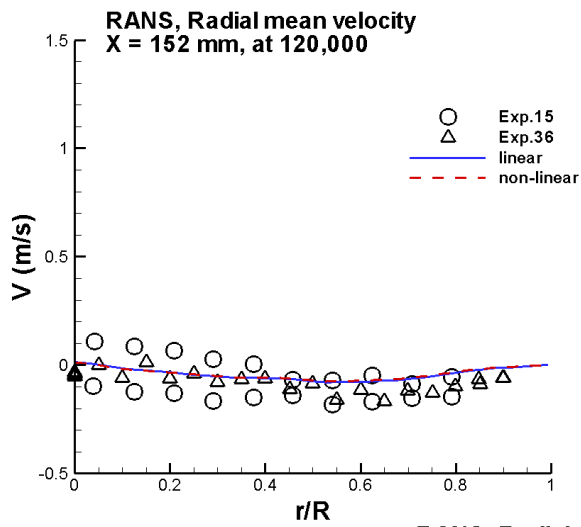


Figure 8.—Concluded.

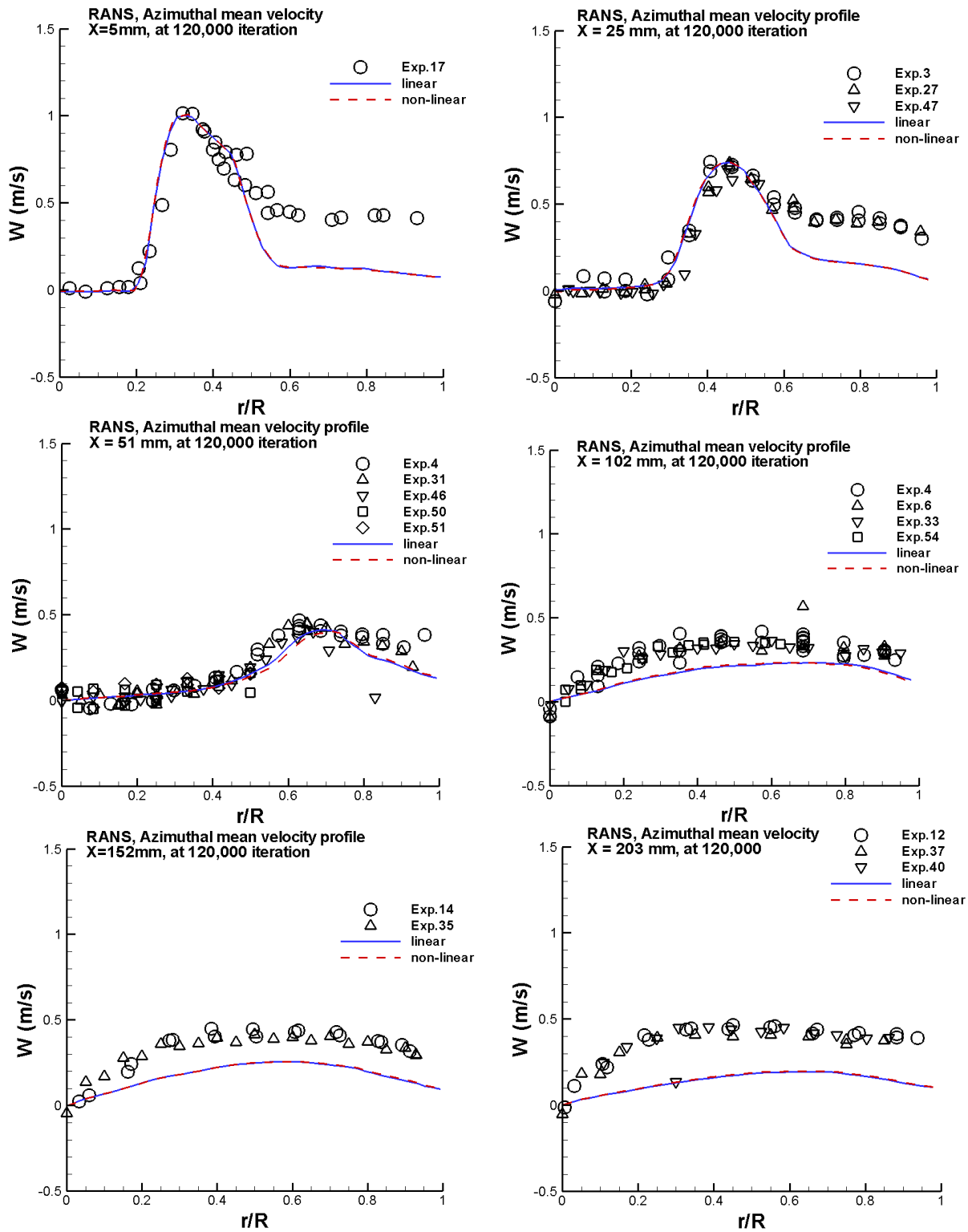


Figure 9.—Radial profiles of azimuthal velocity W at downstream locations.

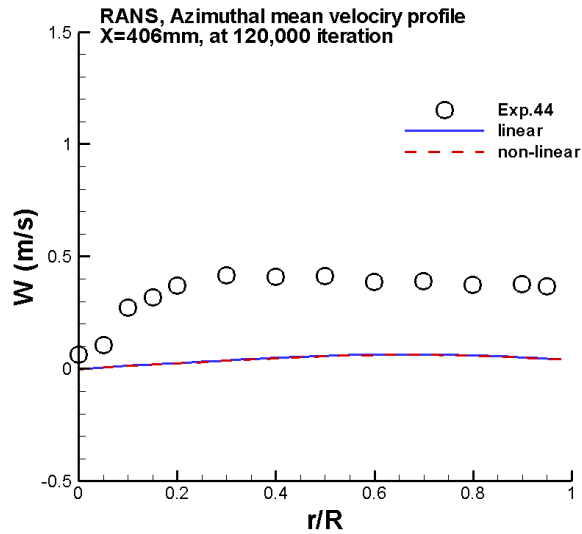


Figure 9.—Concluded.

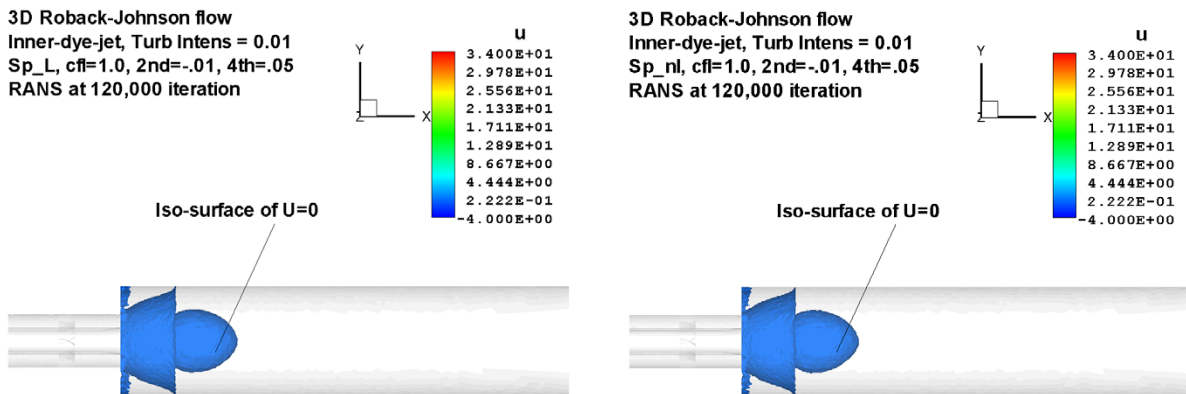
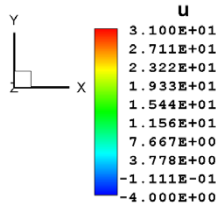


Figure 10.—Comparison of center recirculation zone.

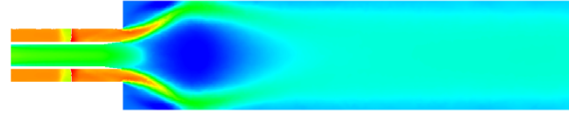
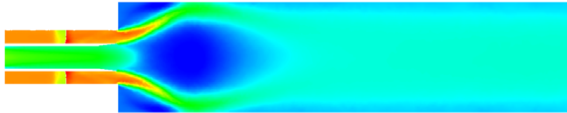
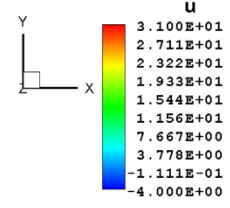
3.1.5 Flow Structure and Contour Plots of Variables in the X-Y Center Plane

To further examine the effects of turbulent scalar flux models (linear vs. nonlinear) on the flow and concentration features, we have plotted the center recirculation zone visualized by the iso-surface of zero axial velocity (see Figure 10), the contour plots of velocity components (Figure 11), the dye mass fraction (Figure 12), the temperature, density, gauge pressure and Mach number (Figure 13), the turbulent kinetic energy and its dissipation rate, and the effective viscosity (Figure 14). The comparisons of these various quantities indicate that, for the current steady RANS simulations of nonreacting flow, the differences in effects due to the linear and nonlinear scalar flux model are negligible.

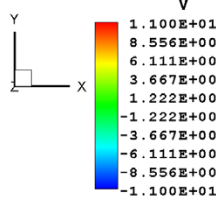
3D Roback-Johnson flow
 Inner-dye-jet, Turb Intens = 0.01
 Sp_L, cfl=1.0, 2nd=-.01, 4th=.05
 RANS at 120,000 iteration



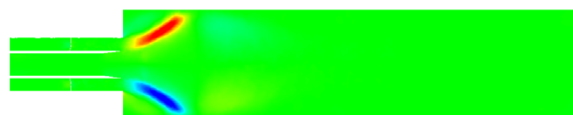
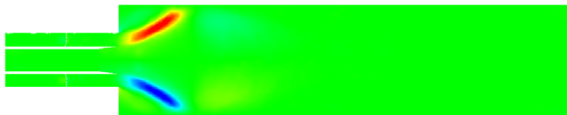
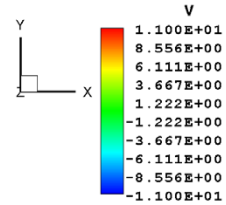
3D Roback-Johnson flow
 Inner-dye-jet, Turb Intens = 0.01
 Sp_nl, cfl=1.0, 2nd=-.01, 4th=.05
 RANS at 120,000 iteration



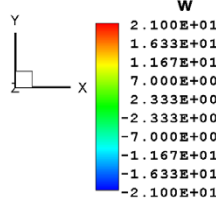
3D Roback-Johnson flow
 Inner-dye-jet, Turb Intens = 0.01
 Sp_L, cfl=1.0, 2nd=-.01, 4th=.05
 RANS at 120,000 iteration



3D Roback-Johnson flow
 Inner-dye-jet, Turb Intens = 0.01
 Sp_nl, cfl=1.0, 2nd=-.01, 4th=.05
 RANS at 120,000 iteration



3D Roback-Johnson flow
 Inner-dye-jet, Turb Intens = 0.01
 Sp_L, cfl=1.0, 2nd=-.01, 4th=.05
 RANS at 120,000 iteration



3D Roback-Johnson flow
 Inner-dye-jet, Turb Intens = 0.01
 Sp_nl, cfl=1.0, 2nd=-.01, 4th=.05
 RANS at 120,000 iteration

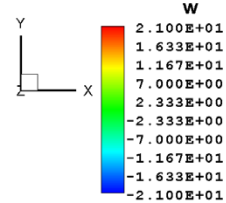
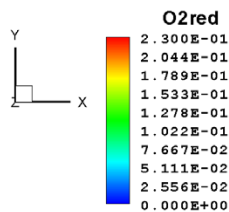


Figure 11.—Comparisons of U,V,W contours in center plane.

3D Roback-Johnson flow
 Inner-dye-jet, Turb Intens = 0.01
 Sp_L, cfl=1.0, 2nd=-.01, 4th=.05
 RANS at 120,000 iteration



3D Roback-Johnson flow
 Inner-dye-jet, Turb Intens = 0.01
 Sp_nl, cfl=1.0, 2nd=-.01, 4th=.05
 RANS at 120,000 iteration

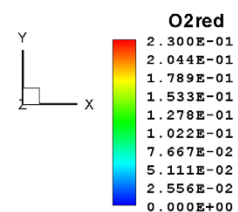
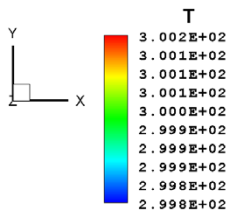
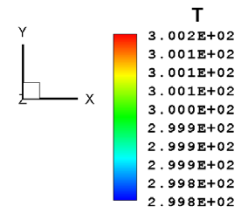


Figure 12.—Comparisons of O₂ mass fraction of the dye in center plane.

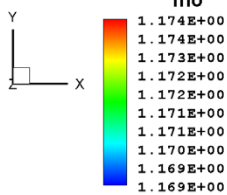
3D Roback-Johnson flow
 Inner-dye-jet, Turb Intens = 0.01
 Sp_L, cfl=1.0, 2nd=-.01, 4th=.05
 RANS at 120,000 iteration



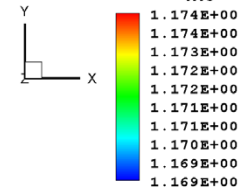
3D Roback-Johnson flow
 Inner-dye-jet, Turb Intens = 0.01
 Sp_nI, cfl=1.0, 2nd=-.01, 4th=.05
 RANS at 120,000 iteration



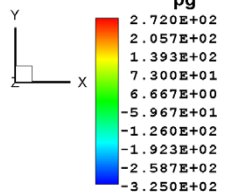
3D Roback-Johnson flow
 Inner-dye-jet, Turb Intens = 0.01
 Sp_L, cfl=1.0, 2nd=-.01, 4th=.05
 RANS at 120,000 iteration



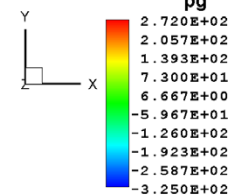
3D Roback-Johnson flow
 Inner-dye-jet, Turb Intens = 0.01
 Sp_nI, cfl=1.0, 2nd=-.01, 4th=.05
 RANS at 120,000 iteration



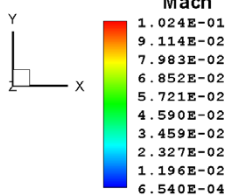
3D Roback-Johnson flow
 Inner-dye-jet, Turb Intens = 0.01
 Sp_L, cfl=1.0, 2nd=-.01, 4th=.05
 RANS at 120,000 iteration



3D Roback-Johnson flow
 Inner-dye-jet, Turb Intens = 0.01
 Sp_nI, cfl=1.0, 2nd=-.01, 4th=.05
 RANS at 120,000 iteration



3D Roback-Johnson flow
 Inner-dye-jet, Turb Intens = 0.01
 Sp_L, cfl=1.0, 2nd=-.01, 4th=.05
 RANS at 120,000 iteration



3D Roback-Johnson flow
 Inner-dye-jet, Turb Intens = 0.01
 Sp_nI, cfl=1.0, 2nd=-.01, 4th=.05
 RANS at 120,000 iteration

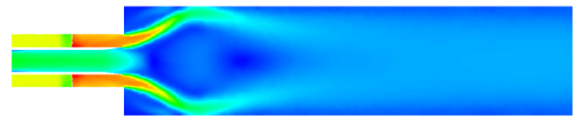
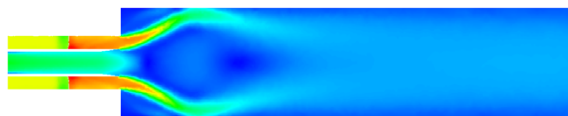
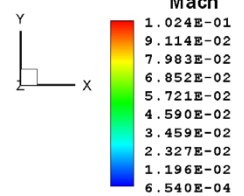
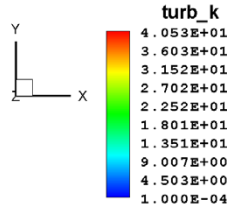
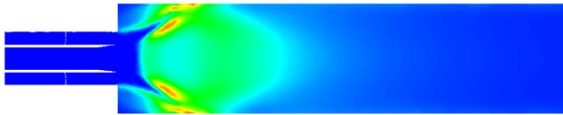
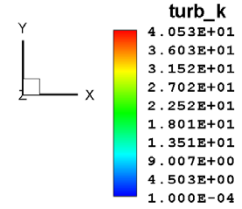


Figure 13.—Comparisons of temperature, density, pressure and Mach number in center plane.

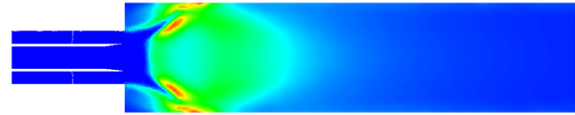
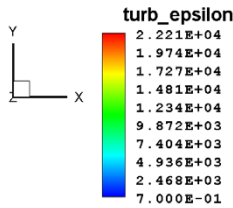
3D Roback-Johnson flow
Inner-dye-jet, Turb Intens = 0.01
Sp_L, cff=1.0, 2nd=-.01, 4th=.05
RANS at 120,000 iteration



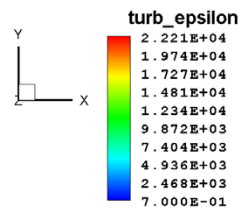
3D Roback-Johnson flow
Inner-dye-jet, Turb Intens = 0.01
Sp_nl, cff=1.0, 2nd=-.01, 4th=.05
RANS at 120,000 iteration



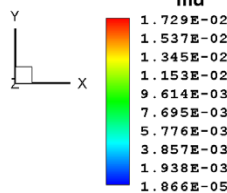
3D Roback-Johnson flow
Inner-dye-jet, Turb Intens = 0.01
Sp_L, cff=1.0, 2nd=-.01, 4th=.05
RANS at 120,000 iteration



3D Roback-Johnson flow
Inner-dye-jet, Turb Intens = 0.01
Sp_nl, cff=1.0, 2nd=-.01, 4th=.05
RANS at 120,000 iteration



3D Roback-Johnson flow
Inner-dye-jet, Turb Intens = 0.01
Sp_L, cff=1.0, 2nd=-.01, 4th=.05
RANS at 120,000 iteration



3D Roback-Johnson flow
Inner-dye-jet, Turb Intens = 0.01
Sp_nl, cff=1.0, 2nd=-.01, 4th=.05
RANS at 120,000 iteration

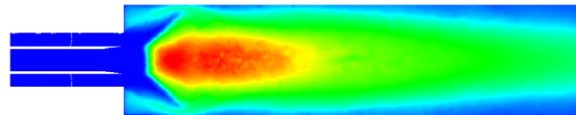
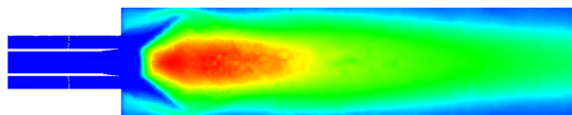
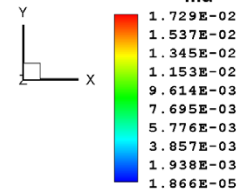


Figure 14.—Comparisons of turbulent kinetic energy, dissipation rate and effective viscosity in center plane.

3.1.6 Remarks

1. Water coaxial jets are satisfactorily simulated by air coaxial jets based on the Reynolds number similarity and under the low speed (nearly incompressible) condition.
2. Concentration of the dye (issued from the inner jet) is well calculated by using both of the linear and the nonlinear species flux models, except in a narrow region near the front stagnation point.
3. Calculations of other flow quantities are also satisfactory:
 - a. Axial and radial velocity components (U and V) are close to the experimental data; however the azimuthal velocity decays too fast towards downstream and significantly lower than the experimental data in the rear half part of the flow.
 - b. The center recirculation bubble is shorter than the measurement by 25 percent.
4. The nonlinear species flux model has not shown appreciable effects on the concentration field comparing with the results from the linear model.

3.2 Results of URANS Simulations With Linear and Nonlinear Scalar Flux Models

In this section, we compare the unsteady RANS (URANS) results obtained from the linear scalar flux model with the results from the nonlinear model. The URANS calculations use the RANS solutions as their initial conditions. The numerical parameter setting for the NCC are: $dt=1.0 \times 10^{-5}$, $cfl=2.0$, inner iteration convergence-criteria= 1.0×10^{-1} , 2nd-smoothing-coeff = -0.01, and 4th-smoothing-coeff = 0.05. When the simulation becomes statistically steady, the mean flow variables are established by averaging over the last 10,000 time steps of the calculation.

The global feature of the simulations is shown in Figure 15, the left one is URANS with the linear scalar flux model, the right one is URANS with the nonlinear scalar flux model. More detailed results and comparisons follow.

3.2.1 Centerline Distributions of Mean Axial Velocity and the Dye Concentration

Figure 16 indicate that both models yield results which are consistent with the experimental data, and the differences of their results are not appreciable.

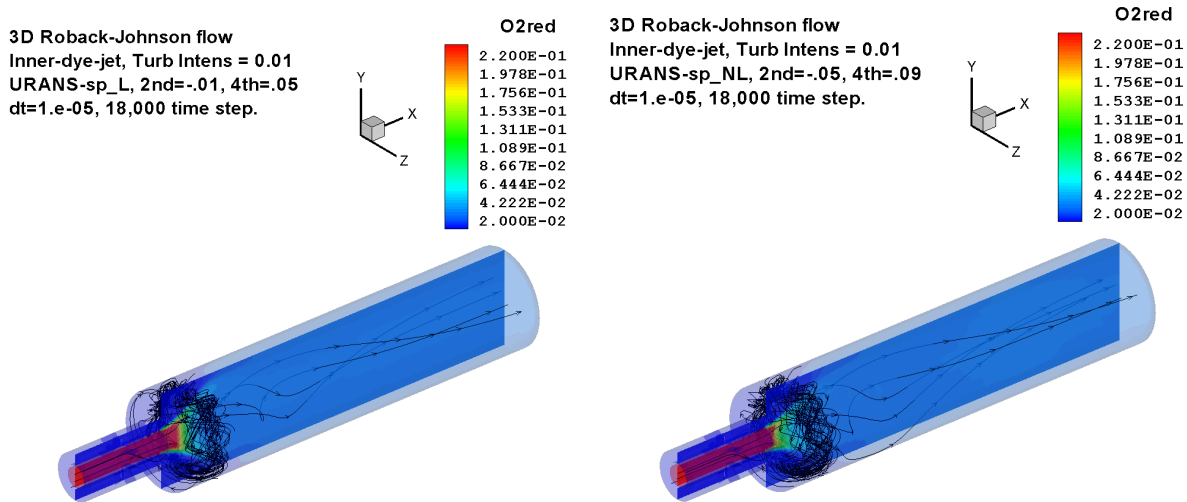


Figure 15.—Global features of URANS with linear vs. nonlinear scalar flux models.

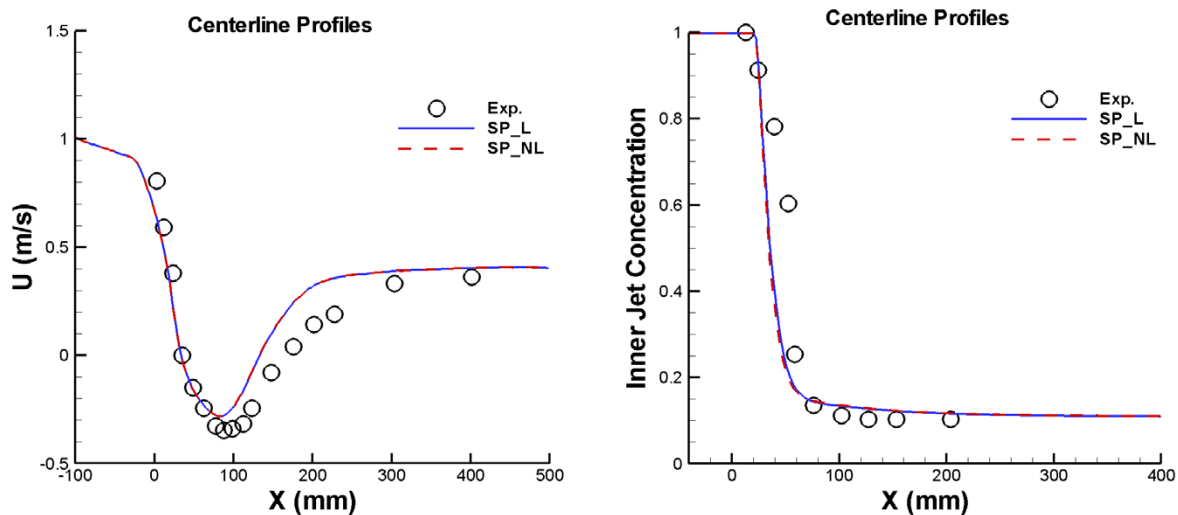


Figure 16.—Centerline distribution of mean axial velocity U and mean dye concentration.

3.2.2 Radial Profiles of the Mean Concentration at Downstream Locations

The radial profiles of the dye concentration at six downstream locations ($x = 13, 25, 51, 102, 152,$ and 203 mm) are shown in Figure 17. Again, the results from both models match the experimental data reasonably well, except for at the location $x = 51$ mm, and the differences among their results are negligible.

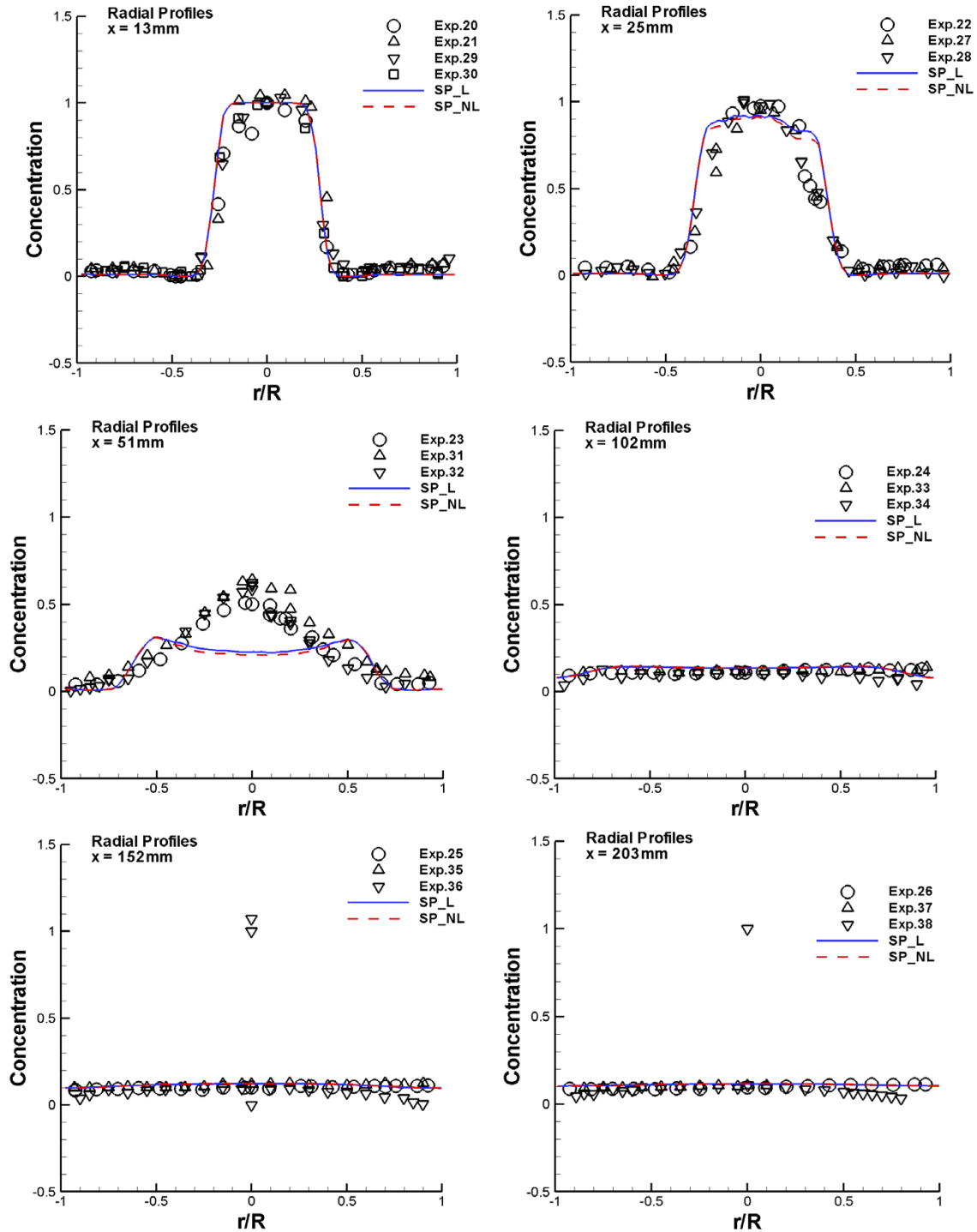


Figure 17.—Radial distributions of dye concentration at downstream locations.

3.2.3 Radial Distribution of Mean Velocity Components U , V , W at Downstream Locations

The radial profiles of axial velocity U , radial velocity V and azimuthal velocity W at eight downstream locations ($x = 5, 25, 51, 102, 152, 203, 305, 406$ mm) are presented in Figure 18, Figure 19 and Figure 20. Results from both models match the experimental data quite well, except for the azimuthal velocity W at the further downstream locations $x = 203 - 406$ mm, where the computed W are under predicted compared with the experimental data.

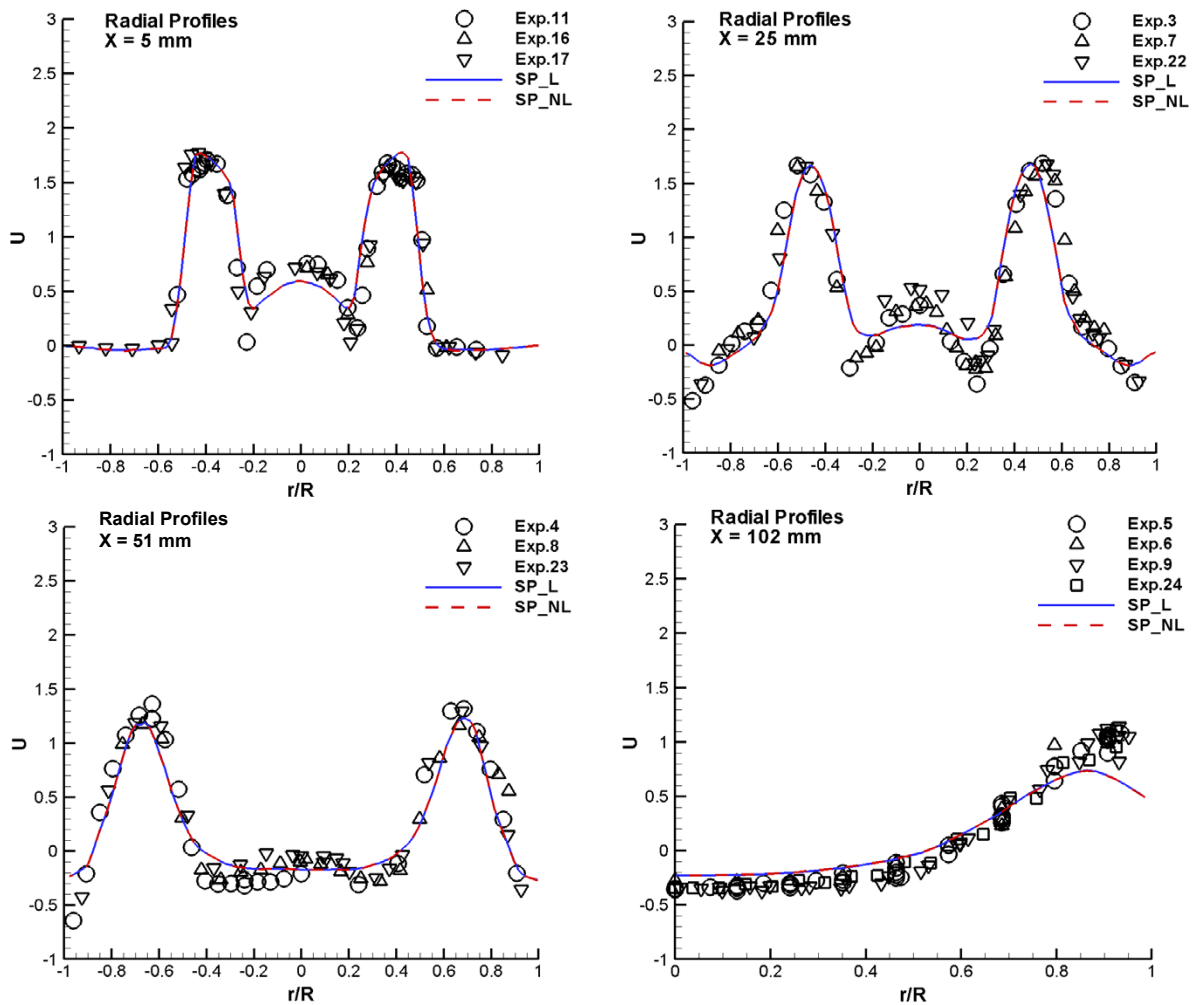


Figure 18.—Radial distributions of mean axial velocity at downstream locations.

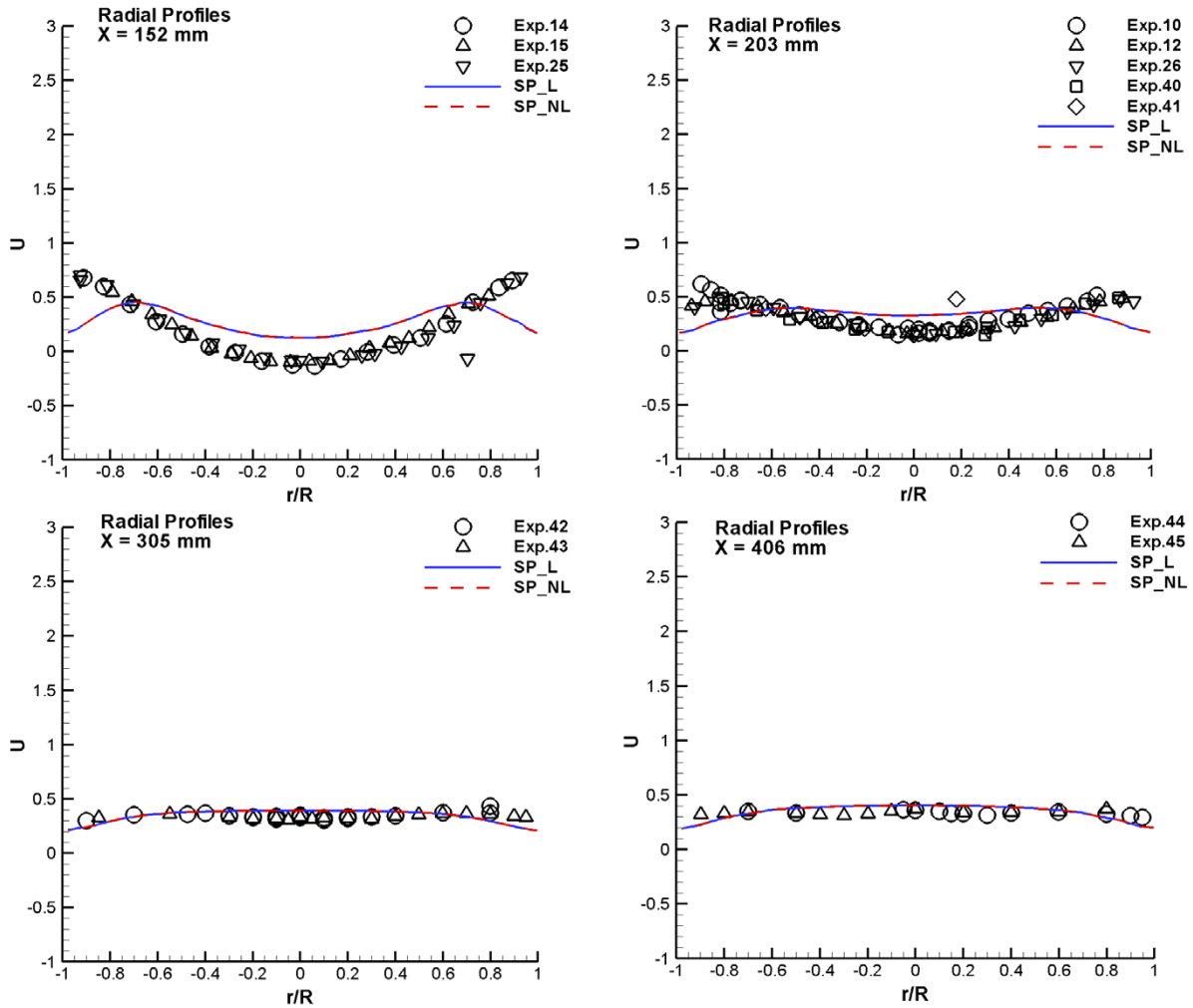


Figure 18.—Concluded.

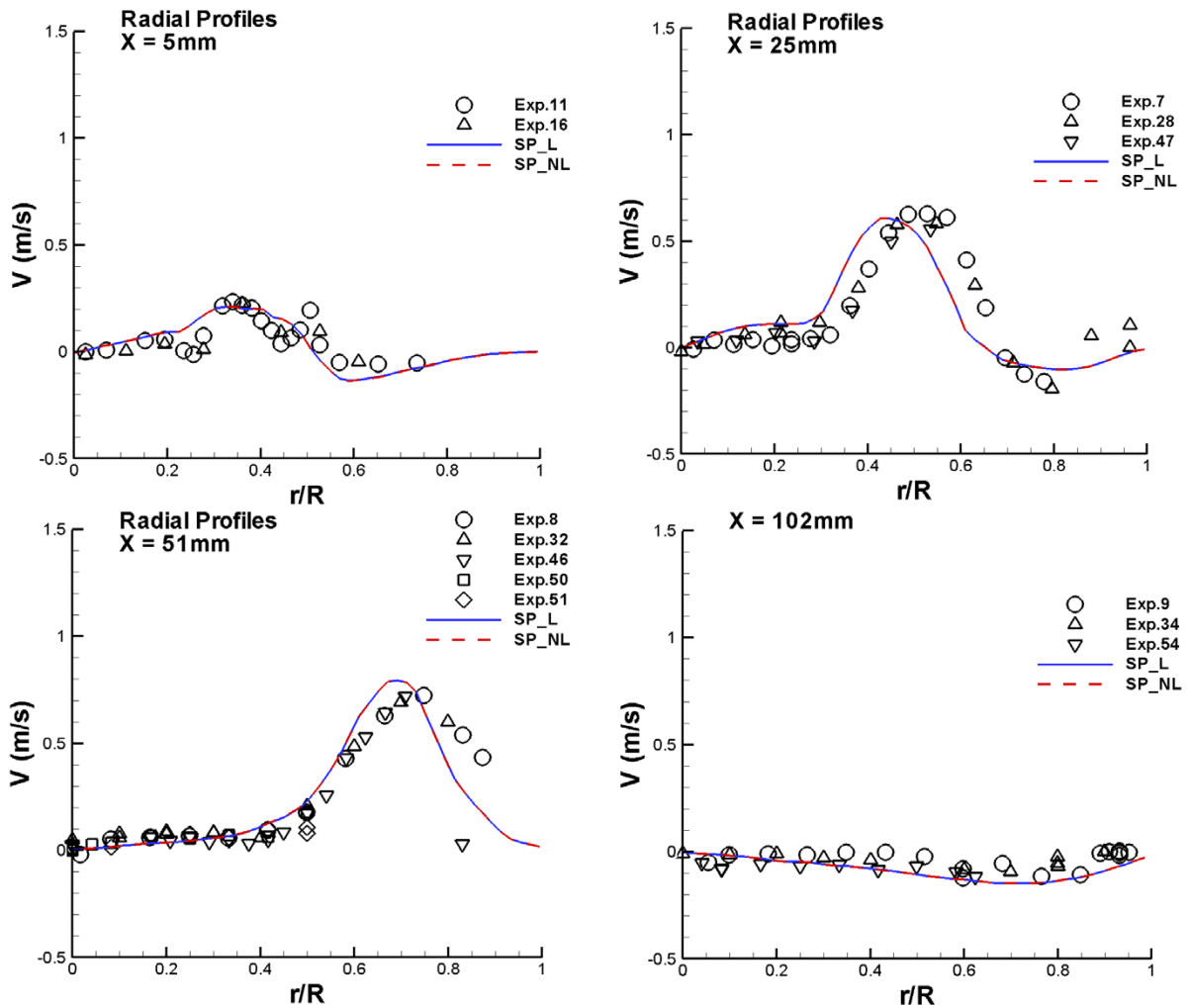


Figure 19.—Radial distributions of mean radial velocity at downstream locations.

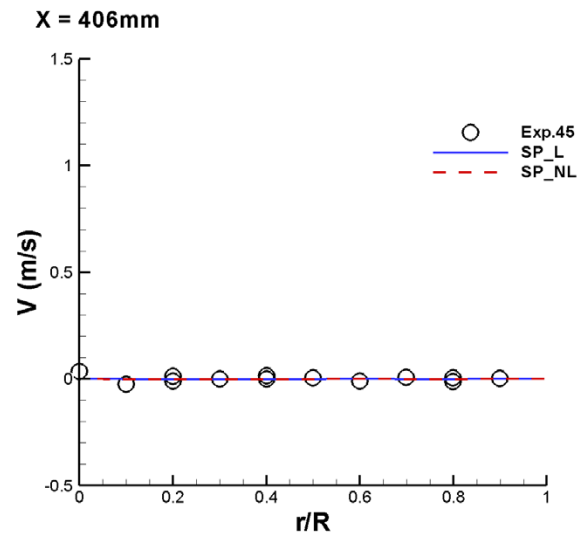
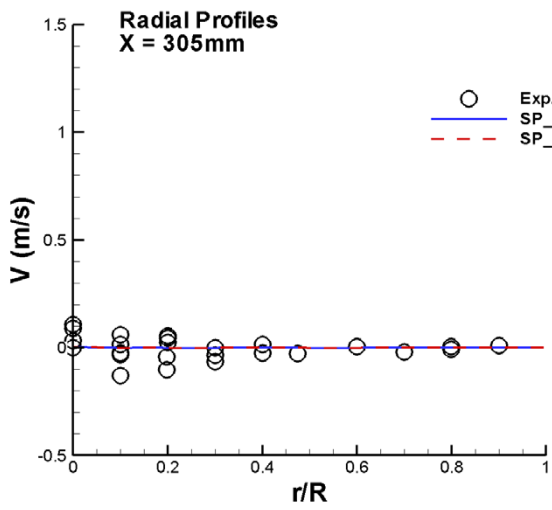
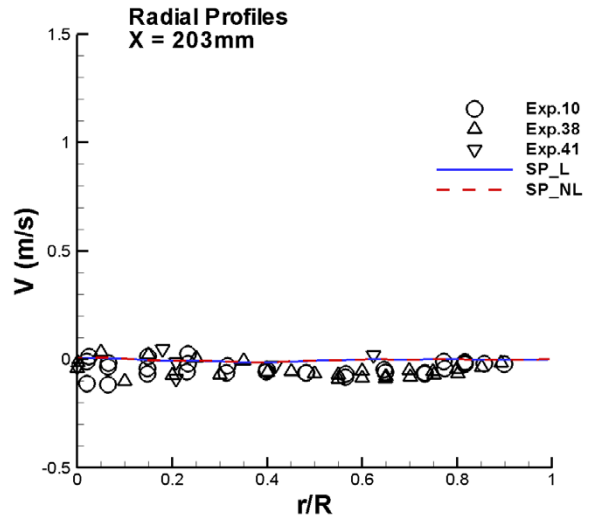
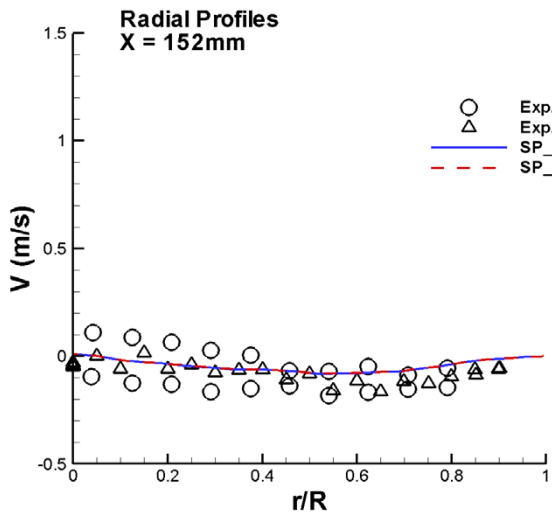


Figure 19.—Concluded.

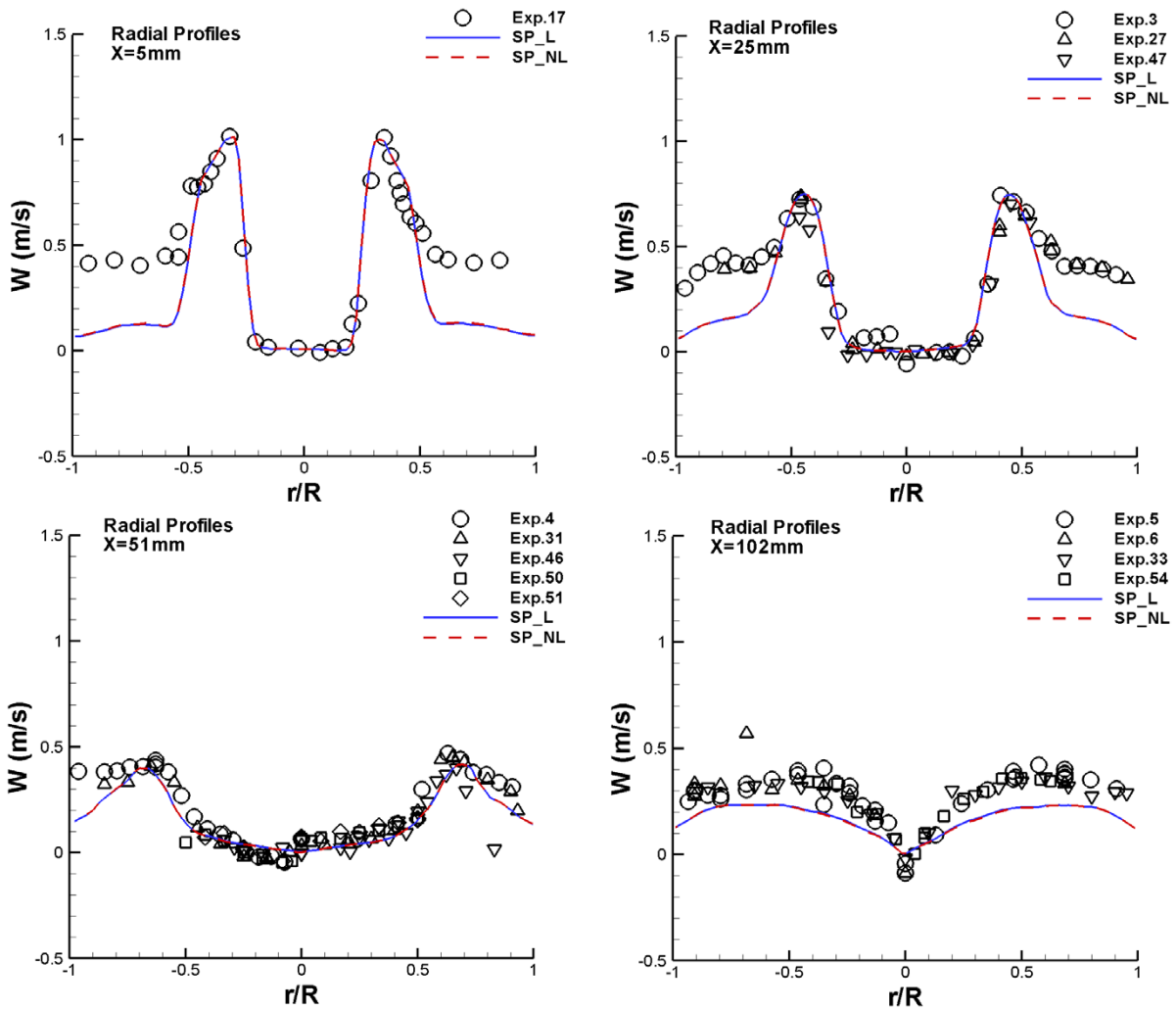


Figure 20.—Comparison of azimuthal velocity component W at downstream locations.

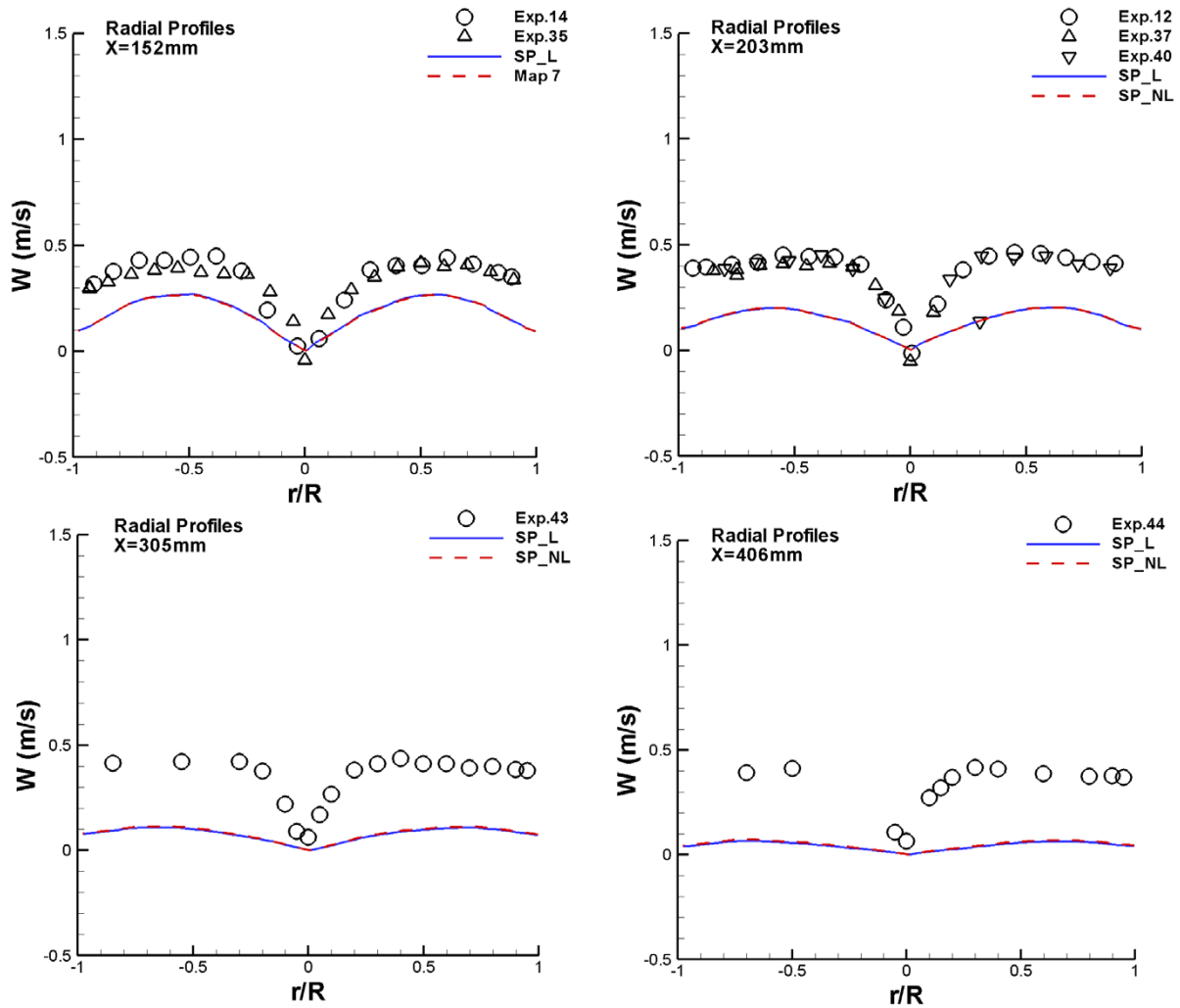
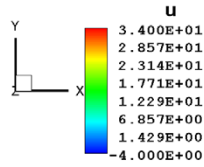


Figure 20.—Concluded.

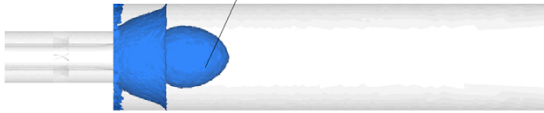
3.2.4 Flow Feature and Contour Plots of Variables in the X-Y Center Plane

To further examine the effects of turbulent scalar flux models on the flow features, we have plotted the center recirculation zone visualized by the iso-surface of zero axial velocity (Figure 21), the contour plots of velocity components (Figure 22), the dye mass fraction and turbulent kinetic energy (Figure 23), the density and temperature (Figure 24). The comparisons of these variables indicate that, for the current URANS simulations of nonreacting flow, the differences of results due to the two scalar flux models are negligible.

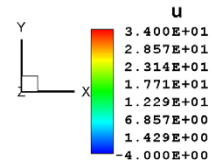
3D Roback-Johnson flow
 Inner-dye-jet, Turb Intens = 0.01
 URANS-sp_L, 2nd=-.01, 4th=.05
 dt=1.e-05, mean,18,000 time step.



Iso-surface of U=0



3D Roback-Johnson flow
 Inner-dye-jet, Turb Intens = 0.01
 URANS-sp_nL, 2nd=-.01, 4th=.05
 dt=1.e-05, 12,000 time step.



Iso-surface of U=0

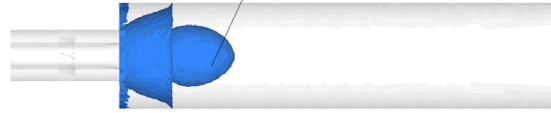
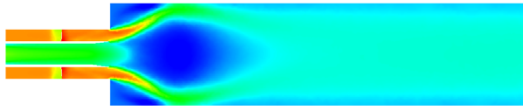
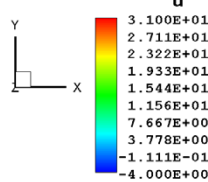
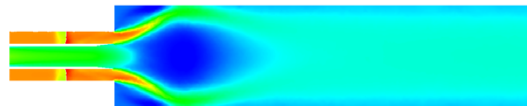
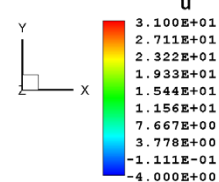


Figure 21.—Comparison of center recirculation zone.

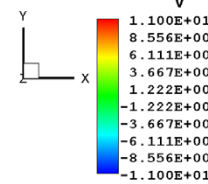
3D Roback-Johnson flow
 Inner-dye-jet, Turb Intens = 0.01
 URANS-sp_L, 2nd=-.01, 4th=.05
 dt=1.e-05, mean,18,000 time step.



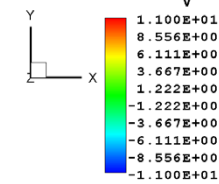
3D Roback-Johnson flow
 Inner-dye-jet, Turb Intens = 0.01
 URANS-sp_nL, 2nd=-.01, 4th=.05
 dt=1.e-05, 12,000 time step.



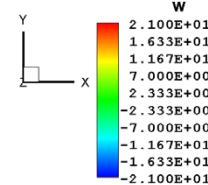
3D Roback-Johnson flow
 Inner-dye-jet, Turb Intens = 0.01
 URANS-sp_L, 2nd=-.01, 4th=.05
 dt=1.e-05, mean,18,000 time step.



3D Roback-Johnson flow
 Inner-dye-jet, Turb Intens = 0.01
 URANS-sp_nL, 2nd=-.01, 4th=.05
 dt=1.e-05, 12,000 time step.



3D Roback-Johnson flow
 Inner-dye-jet, Turb Intens = 0.01
 URANS-sp_L, 2nd=-.01, 4th=.05
 dt=1.e-05, mean,18,000 time step.



3D Roback-Johnson flow
 Inner-dye-jet, Turb Intens = 0.01
 URANS-sp_nL, 2nd=-.01, 4th=.05
 dt=1.e-05, 12,000 time step.

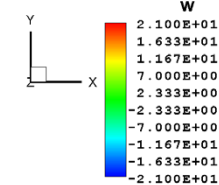
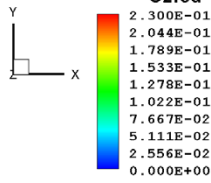
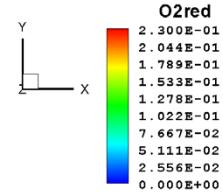


Figure 22.—Comparison of mean velocities U , V , W contours in center plane.

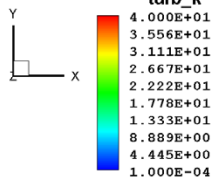
3D Roback-Johnson flow
 Inner-dye-jet, Turb Intens = 0.01
 URANS-sp_L, 2nd=-.01, 4th=.05
 dt=1.e-05, mean,18,000 time step.



3D Roback-Johnson flow
 Inner-dye-jet, Turb Intens = 0.01
 URANS-sp_nL, 2nd=-.01, 4th=.05
 dt=1.e-05, 12,000 time step.



3D Roback-Johnson flow
 Inner-dye-jet, Turb Intens = 0.01
 URANS-sp_L, 2nd=-.01, 4th=.05
 dt=1.e-05, mean,18,000 time step.



3D Roback-Johnson flow
 Inner-dye-jet, Turb Intens = 0.01
 URANS-sp_nL, 2nd=-.01, 4th=.05
 dt=1.e-05, 12,000 time step.

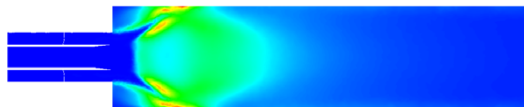
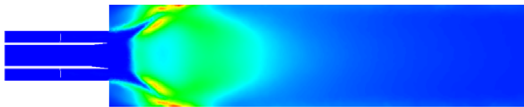
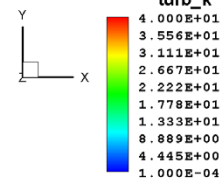
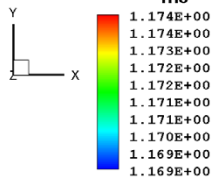
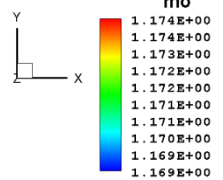


Figure 23.—Comparison of mean O₂ mass fraction of the dye and k contours in center plane.

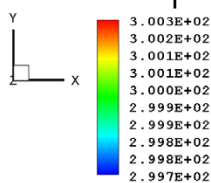
3D Roback-Johnson flow
 Inner-dye-jet, Turb Intens = 0.01
 URANS-sp_L, 2nd=-.01, 4th=.05
 dt=1.e-05, mean,18,000 time step.



3D Roback-Johnson flow
 Inner-dye-jet, Turb Intens = 0.01
 URANS-sp_nL, 2nd=-.01, 4th=.05
 dt=1.e-05, 12,000 time step.



3D Roback-Johnson flow
 Inner-dye-jet, Turb Intens = 0.01
 URANS-sp_L, 2nd=-.01, 4th=.05
 dt=1.e-05, mean,18,000 time step.



3D Roback-Johnson flow
 Inner-dye-jet, Turb Intens = 0.01
 URANS-sp_nL, 2nd=-.01, 4th=.05
 dt=1.e-05, 12,000 time step.

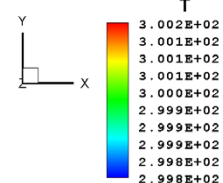


Figure 24.—Comparison of mean density and temperature contours in center plane.

3.2.5 Remarks

1. Concentration of the dye (issued from the inner jet) is satisfactorily calculated by both of the linear and nonlinear species flux models, except in a narrow region near the front stagnation point.
2. Other flow quantities also are satisfactorily calculated:
 - a. Axial and radial velocity components (U and V) are close to the experimental data; however the azimuthal velocity decays too fast towards downstream and significantly lower than the experimental data in the far downstream of the chamber.
 - b. The center recirculation bubble is shorter than its experimental counter part by 25%.
3. The results have not shown appreciable effect of the nonlinear species flux model on the concentration field when compared with the results from the linear model.

3.3 Results of TFNS Simulations With Linear and Nonlinear Scalar Flux Models

In this section, we present and compare the results of TFNS simulations using linear and nonlinear subscale scalar flux models. The TFNS calculations use the URANS solutions as the initial condition. The numerical parameter setting in the NCC is: $dt = 2.0 \times 10^{-6}$, $cfl=1.0$, inner iteration convergence-criteria = 1.0×10^{-1} , 2nd-smoothing-coeff = 0.0, and 4th-smoothing-coeff = 0.05. At the outlet, an unsteady convective boundary condition is employed. The filtering resolution control parameter RCP is set to be 0.25. The same grid used in the RANS and URANS simulations is used for the current TFNS simulations.

The global feature of the TFNS simulations are shown in Figure 25, the left one is TFNS with the linear subscale scalar flux model, the right one is TFNS with the nonlinear subscale scalar flux model. More detailed results and comparisons follow.

3.3.1 Time Variation of Instantaneous Velocity Components at Centerline Probes

Time histories of velocity components at five downstream locations are recorded during the simulations, the last three of probes are shown in Figure 26. The ones on the left are TFNS with the linear subscale scalar flux model; the ones on the right are TFNS with the nonlinear subscale scalar flux model. It can be seen that the turbulent fluctuation quickly develops from the location of probe 3 to the region of probes 4 and 5, so that the simulated flow in the chamber is a fully developed turbulent flow.

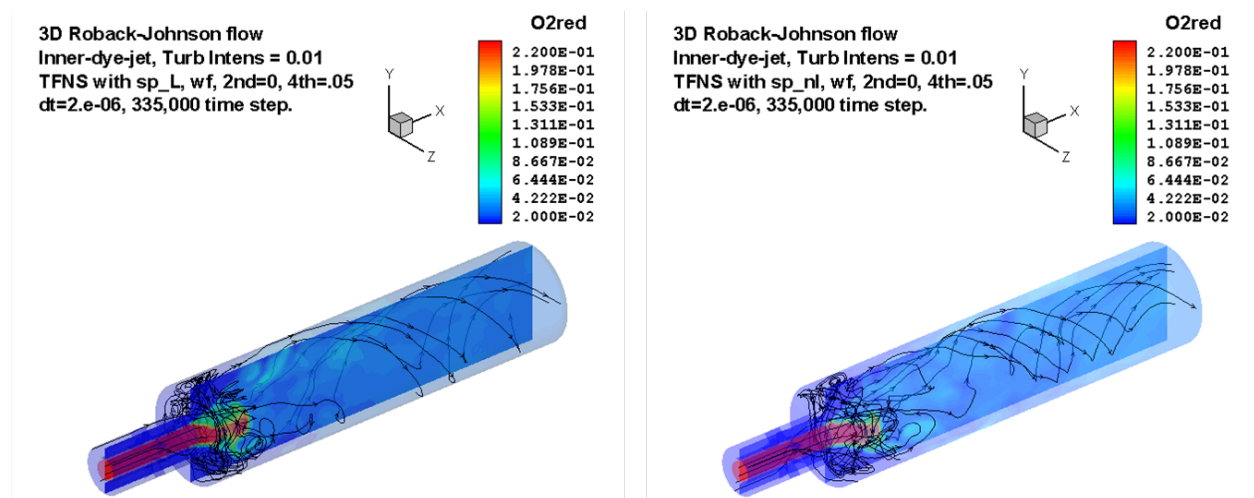


Figure 25.—Global features of TFNS using linear and nonlinear subscale scalar flux models.

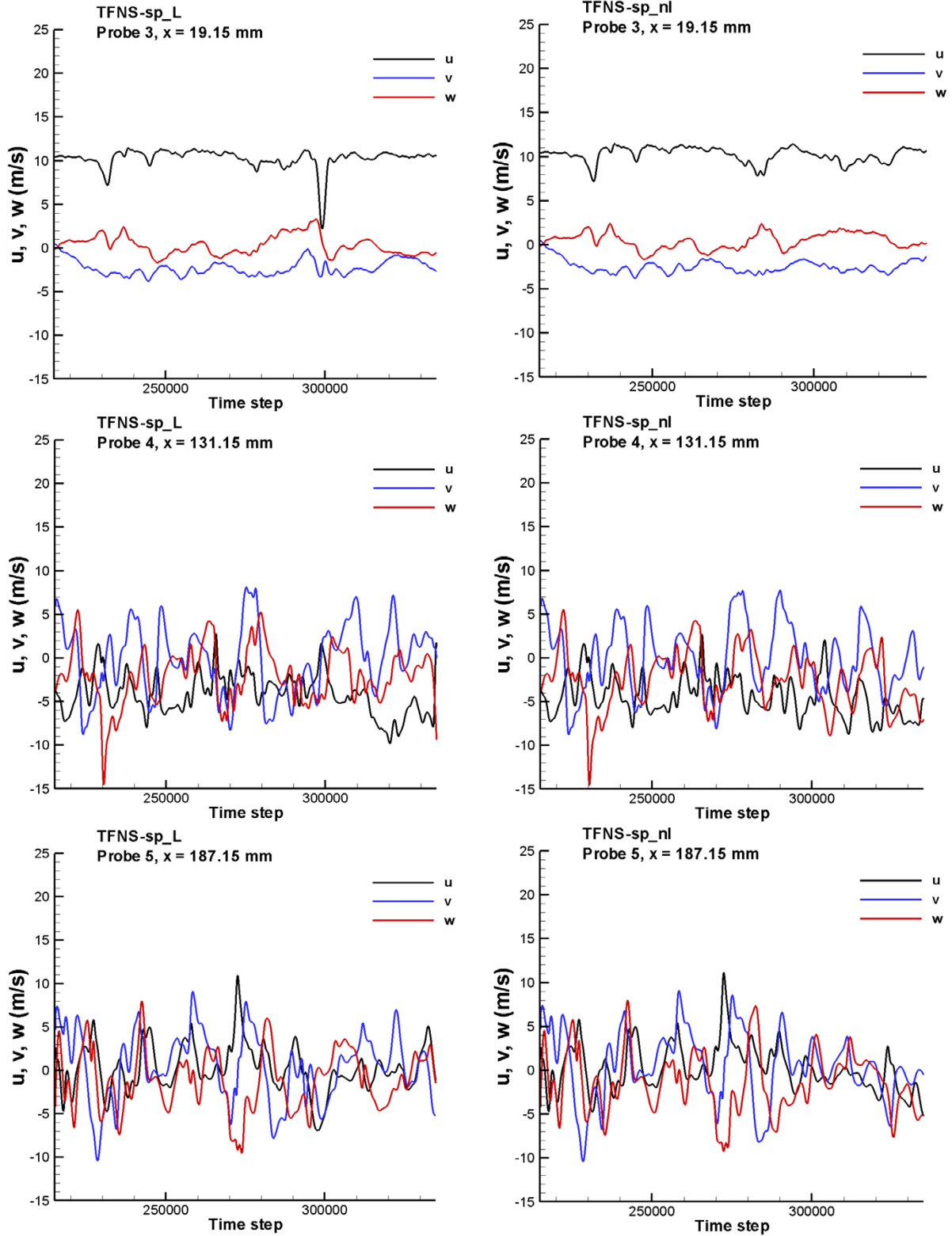


Figure 26.—Time history of velocity components u , v and w at probes 3, 4 and 5.

3.3.2 Centerline Distributions of Mean Axial Velocity and Mean Dye Concentration

Figure 27 indicate that results from both scalar flux models are consistent with the experimental data, and the differences between their results are small, albeit appreciable.

3.3.3 Radial Profiles of Mean Concentration at Downstream Locations

The radial profiles of mean concentration of the dye at six downstream locations ($x = 13, 25, 51, 102, 152, 203$ mm) are shown in Figure 28. Again, results from both models match the experimental data quite well, including those at the location of $x = 51$ mm, and this is a noticeable improvement over the RANS as well as the URANS results. There are small but appreciable differences between the results from the two subscale scalar flux models.

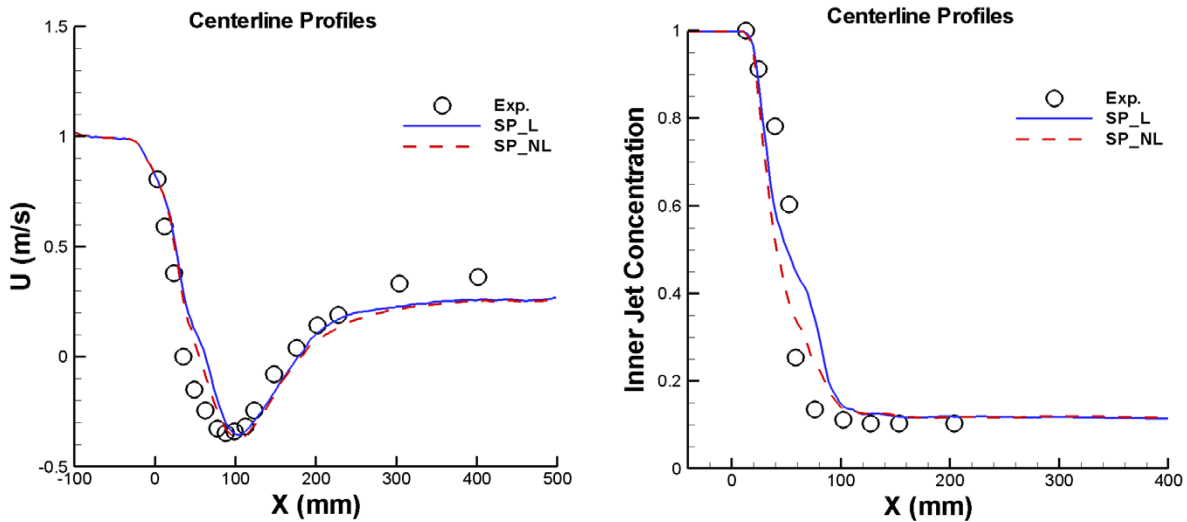


Figure 27.—Centerline distribution of mean axial velocity U and mean concentration of the dye.

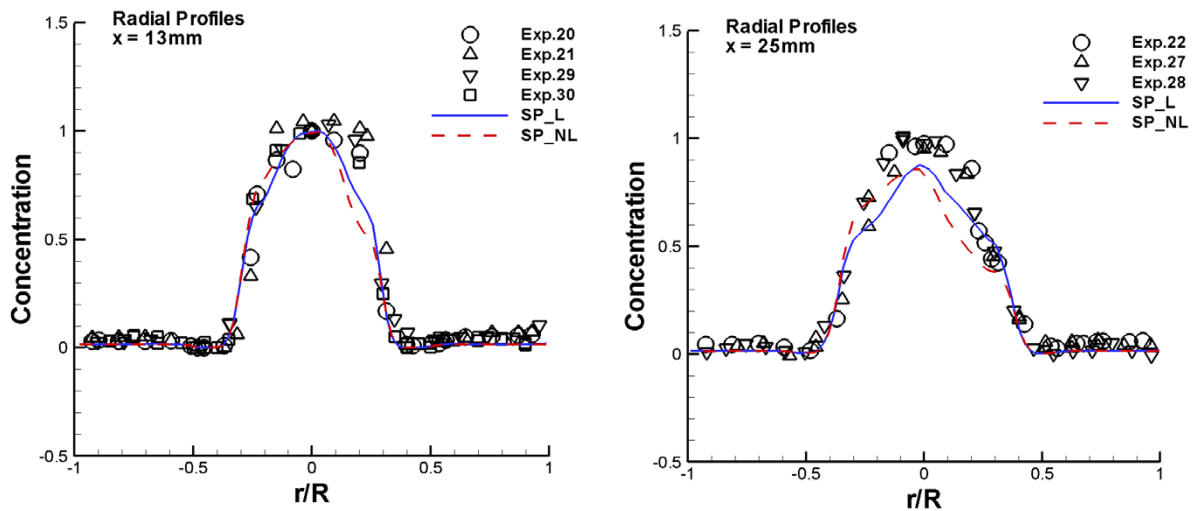


Figure 28.—Radial distributions of mean dye concentration at downstream locations.

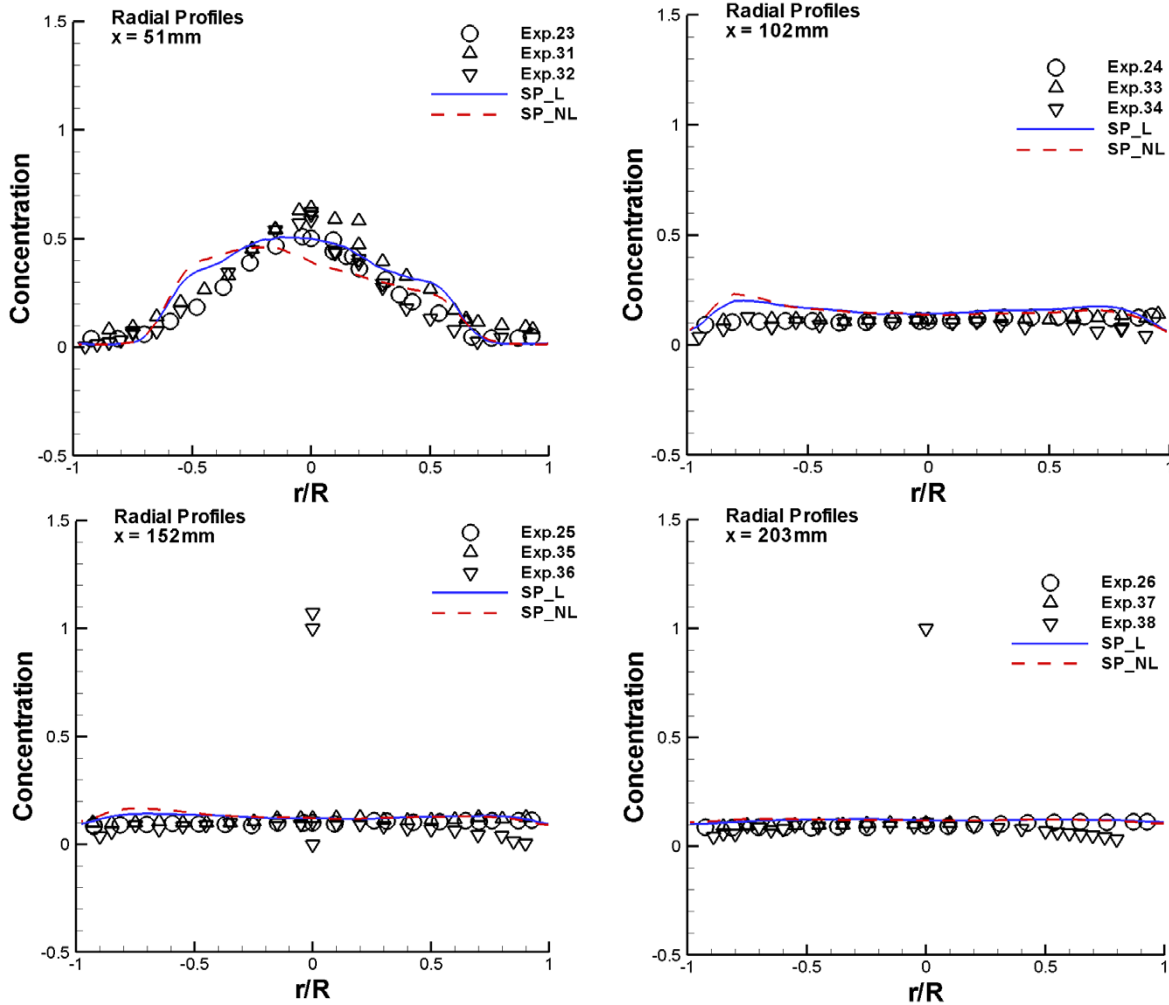


Figure 28.—Concluded.

3.3.4 Radial Profiles of Mean Velocity Components at Downstream Locations

The mean radial profiles of axial velocity U , radial velocity V and azimuthal velocity W at eight downstream locations ($x = 5, 25, 51, 102, 152, 203, 305,$ and 406 mm) are presented in Figure 29, Figure 30 and Figure 31. Results from both models match the experimental data quite well. For the azimuthal velocity W , results from the TFNS simulations show significant improvement over the results from the RANS and the URANS simulations near the wall region of the front chamber ($x=5, 25, 51\text{ mm}$) as well as at the further downstream locations $x = 203 - 406\text{ mm}$. Again, the differences between the results from the two subscale scalar flux models are small.

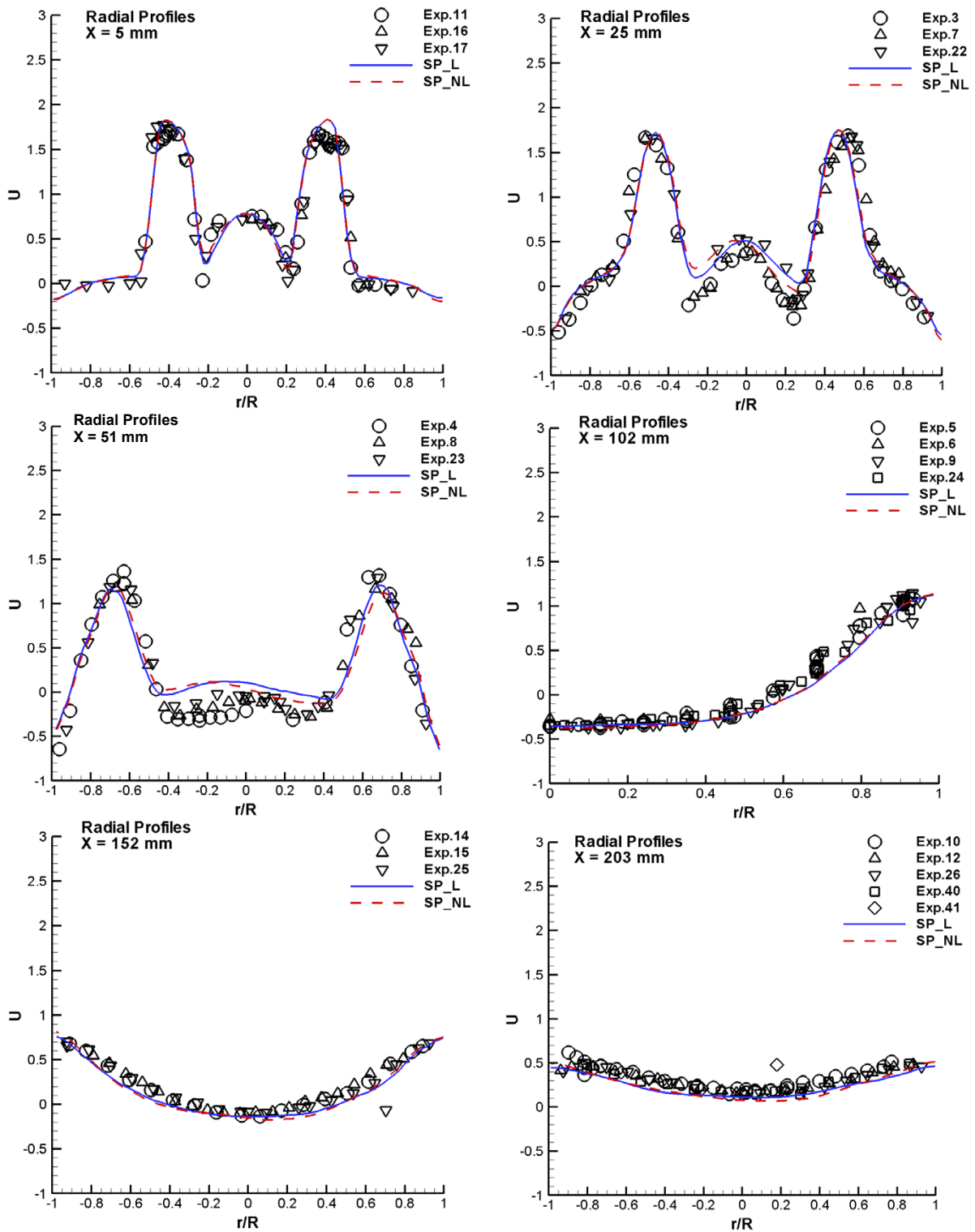


Figure 29.—Radial distributions of mean axial velocity at downstream locations.

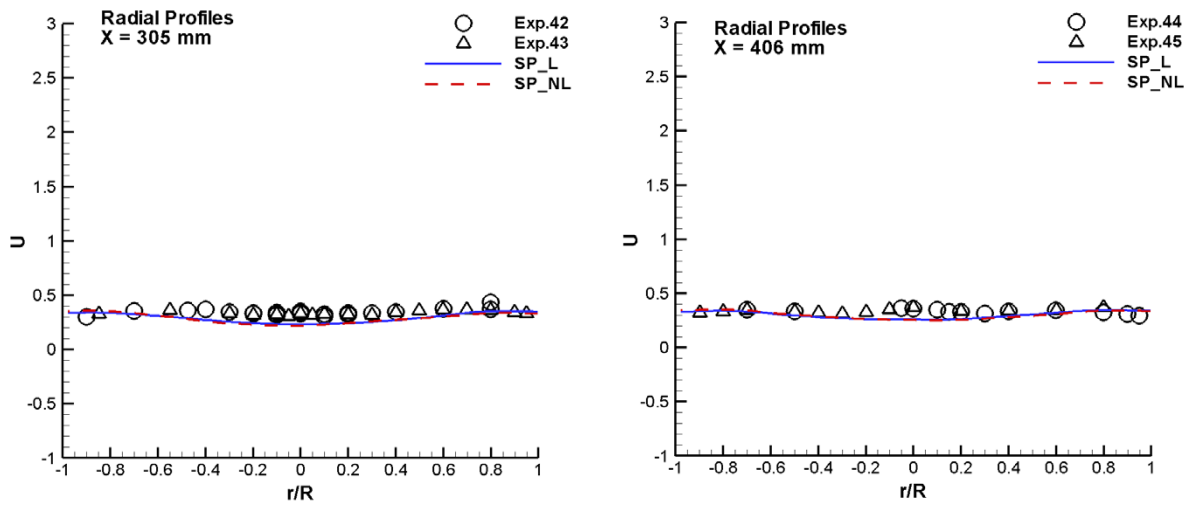


Figure 29.—Concluded.

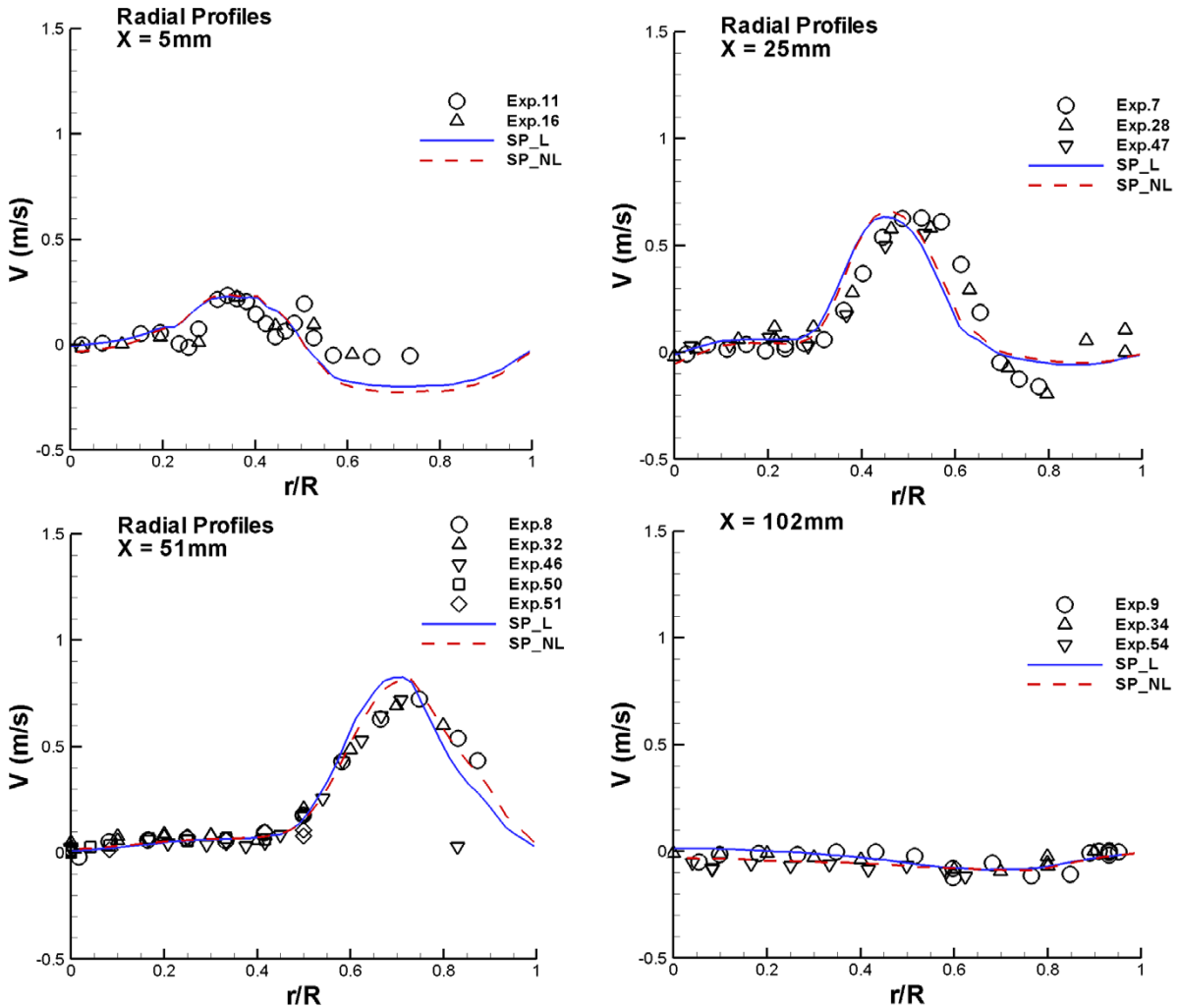


Figure 30.—Radial distributions of mean radial velocity at downstream locations.

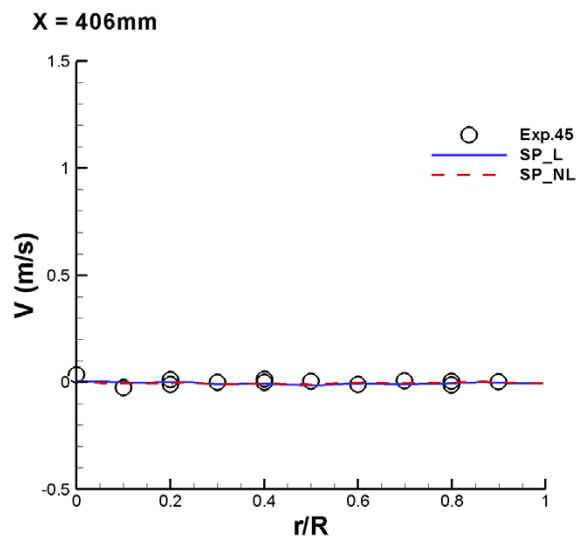
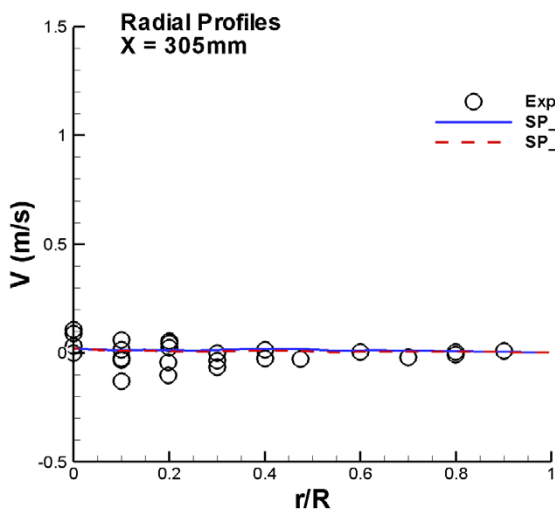
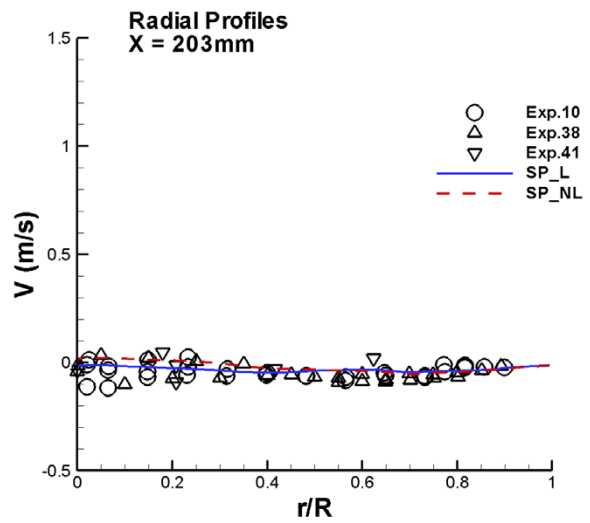
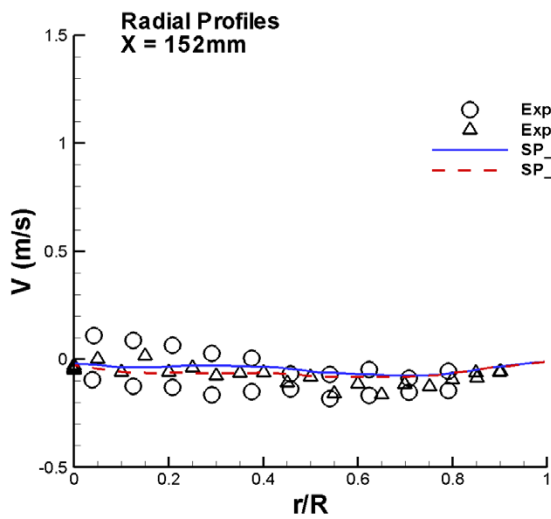


Figure 30.—Concluded.

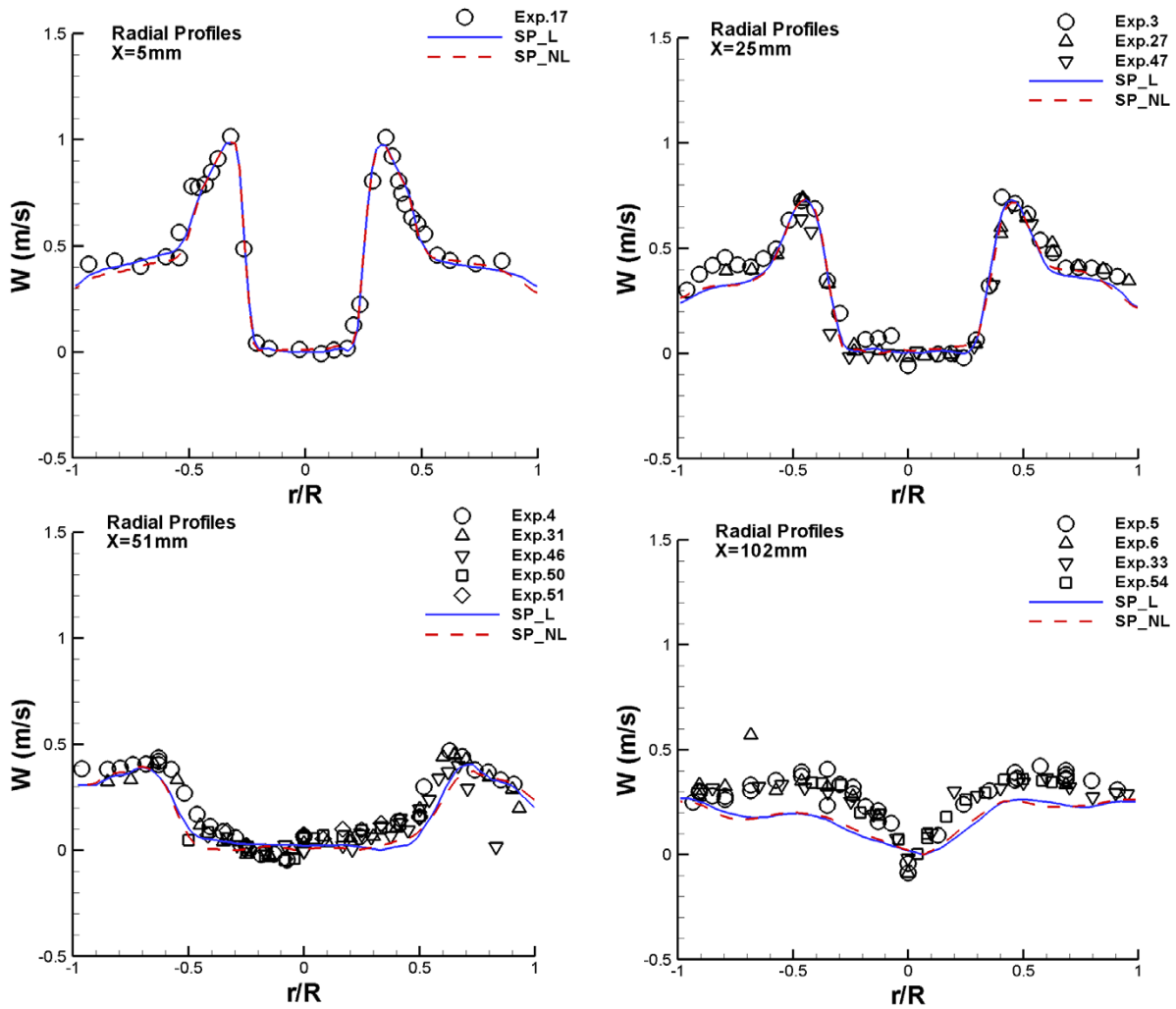


Figure 31.—Radial distributions of mean azimuthal velocity at downstream locations.

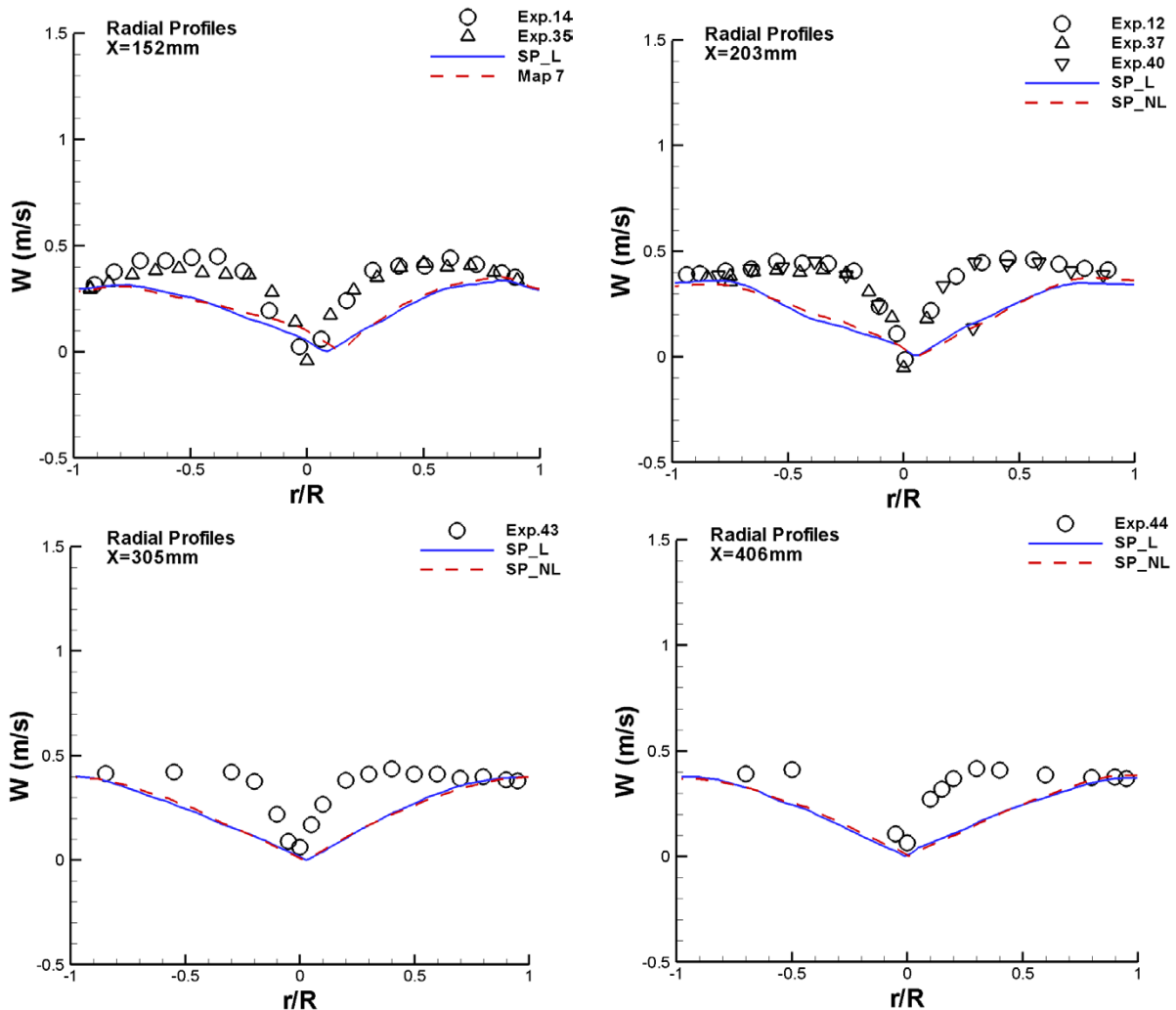


Figure 31.—Concluded.

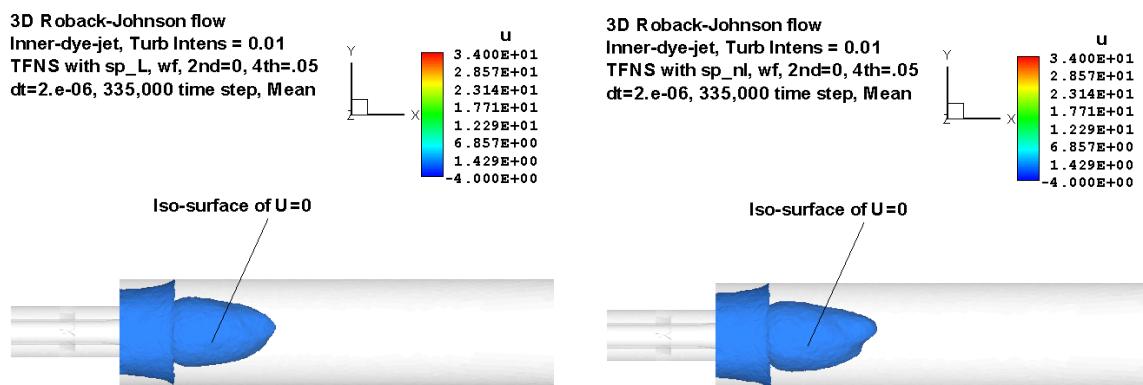


Figure 32.—Comparison of the center recirculation zone.

3.3.5 Mean Flow Structure and Contour Plots of Variables in the X-Y Center Plane

To further examine the effects of the subscale scalar flux models on the mean flow quantities, we have plotted the center recirculation zone visualized by the iso-surface of zero mean axial velocity (Figure 32), the contour plots of mean velocity components and vorticity magnitude (Figure 33), the mean O_2

mass fraction of the dye, the subscale kinetic energy and its dissipation rate (Figure 34). These comparisons indicate that results from these two models are very close.

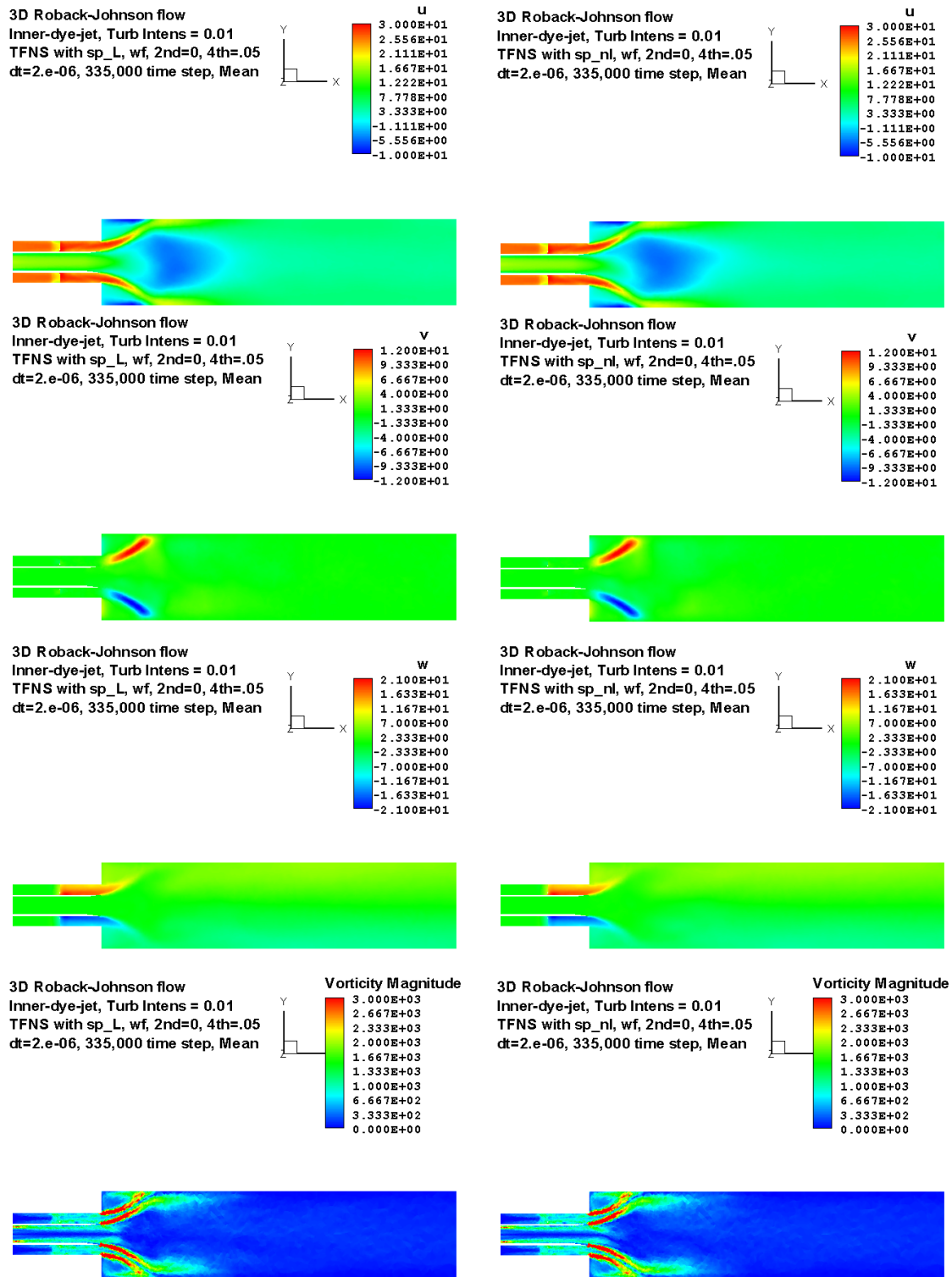


Figure 33.—Comparison of mean velocities U , V , W and vorticity contours in center plane.

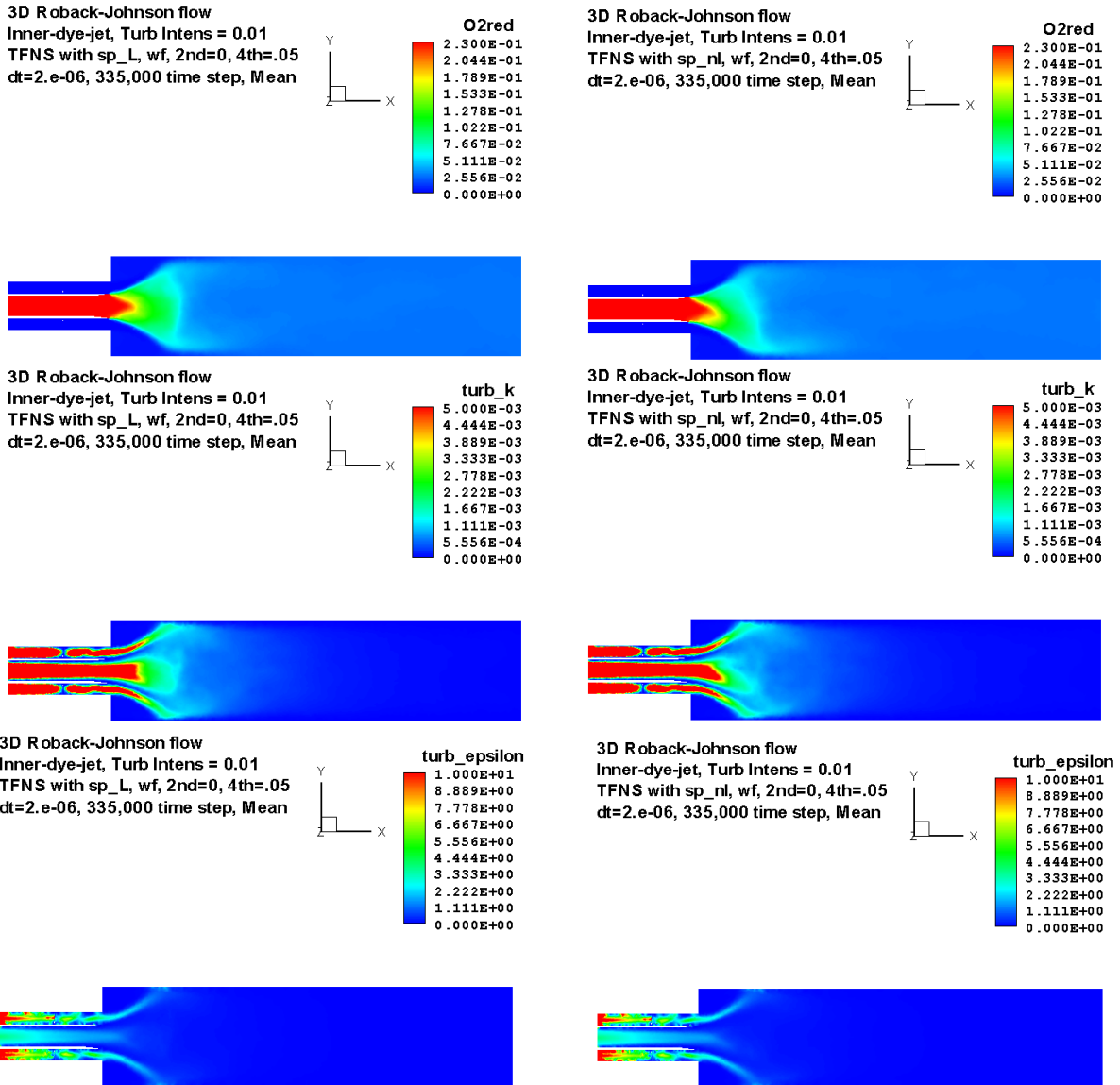
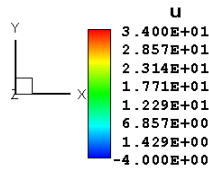


Figure 34.—Distributions of O₂ mass fraction of the dye, subscale kinetic energy and dissipation rate in center plane.

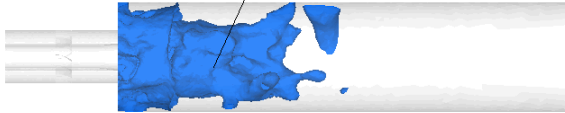
3.3.6 Instantaneous Contour Plots of Variables in the X-Y Center Plane

Additional comparisons in terms of the instantaneous features are presented here. Figure 35 shows the center recirculation zone visualized by the iso-surface of zero axial velocity, the contour plots of instantaneous velocity components, the vorticity magnitude, the O₂ mass fraction of the dye, the subscale kinetic energy, and the effective viscosity $\mu + \mu_T$. Comparison of these snap shots suggests that the nonlinear subscale scalar flux model adds finer details to the unsteady flow features.

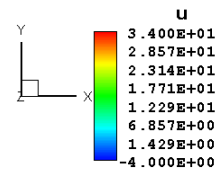
3D Roback-Johnson flow
 Inner-dye-jet, Turb Intens = 0.01
 TFNS with sp_L, wf, 2nd=0, 4th=.05
 dt=2.e-06, at 335,000 time step



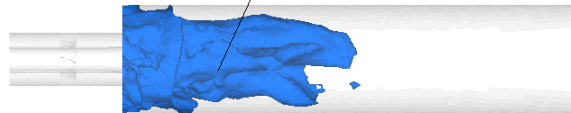
Iso-surface of U=0



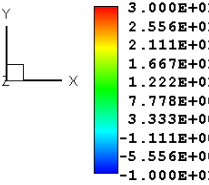
3D Roback-Johnson flow
 Inner-dye-jet, Turb Intens = 0.01
 TFNS with sp_nl, wf, 2nd=0, 4th=.05
 dt=2.e-06, at 335,000 time step



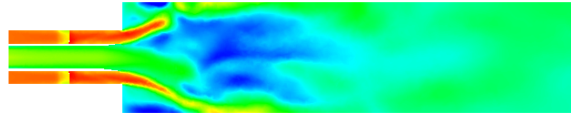
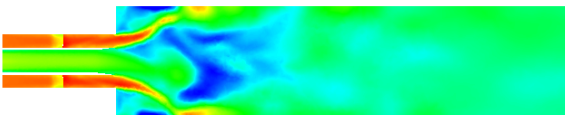
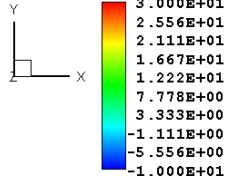
Iso-surface of U=0



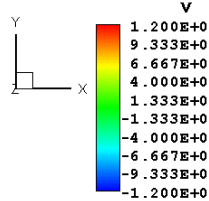
3D Roback-Johnson flow
 Inner-dye-jet, Turb Intens = 0.01
 TFNS with sp_L, wf, 2nd=0, 4th=.05
 dt=2.e-06, at 335,000 time step



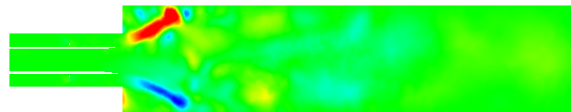
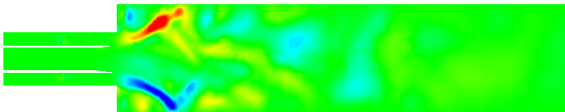
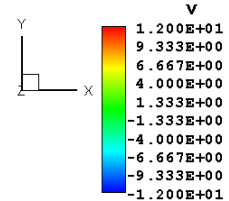
3D Roback-Johnson flow
 Inner-dye-jet, Turb Intens = 0.01
 TFNS with sp_nl, wf, 2nd=0, 4th=.05
 dt=2.e-06, at 335,000 time step



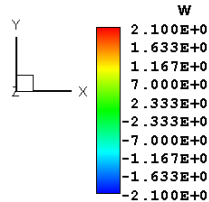
3D Roback-Johnson flow
 Inner-dye-jet, Turb Intens = 0.01
 TFNS with sp_L, wf, 2nd=0, 4th=.05
 dt=2.e-06, at 335,000 time step



3D Roback-Johnson flow
 Inner-dye-jet, Turb Intens = 0.01
 TFNS with sp_nl, wf, 2nd=0, 4th=.05
 dt=2.e-06, at 335,000 time step



3D Roback-Johnson flow
 Inner-dye-jet, Turb Intens = 0.01
 TFNS with sp_L, wf, 2nd=0, 4th=.05
 dt=2.e-06, at 335,000 time step



3D Roback-Johnson flow
 Inner-dye-jet, Turb Intens = 0.01
 TFNS with sp_nl, wf, 2nd=0, 4th=.05
 dt=2.e-06, at 335,000 time step

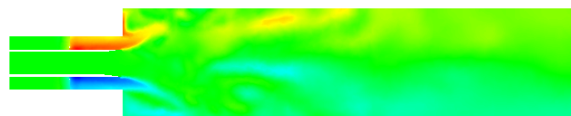
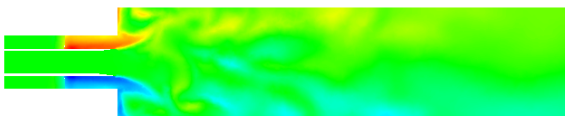
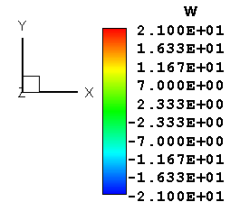


Figure 35.—Contours of instantaneous variables in X-Y center plane.

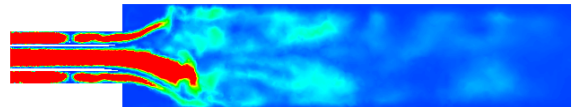
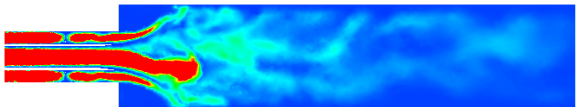
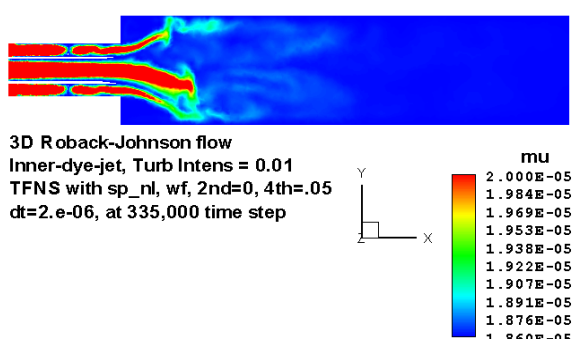
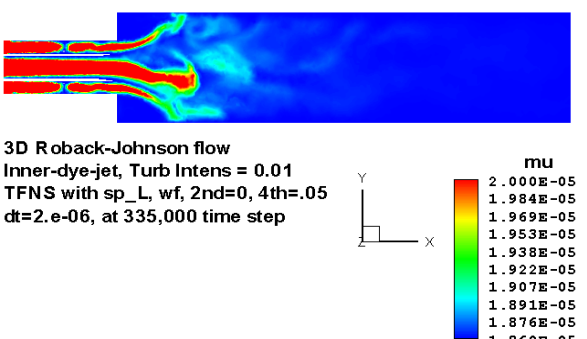
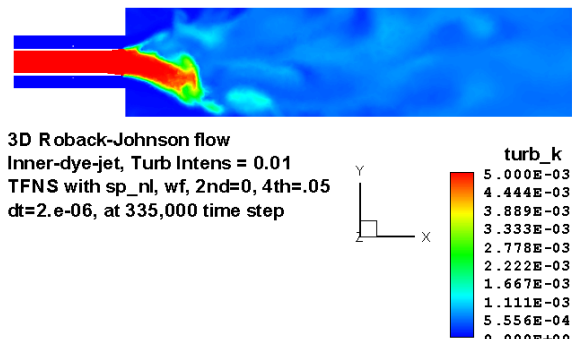
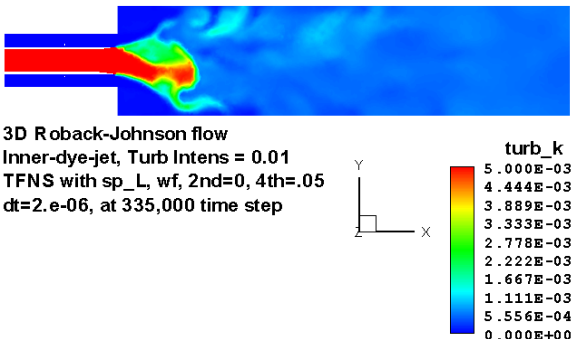
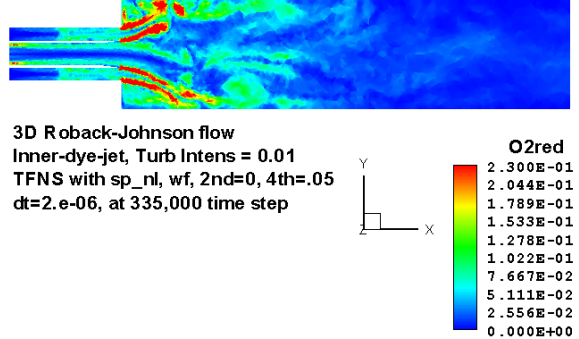
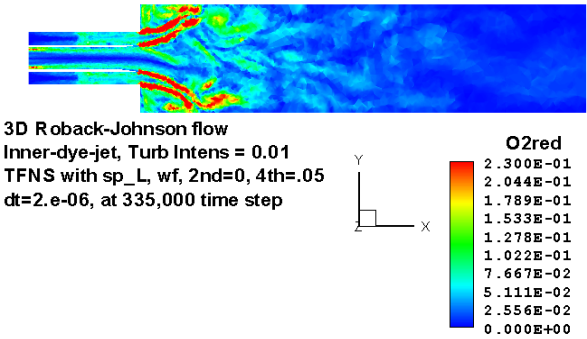
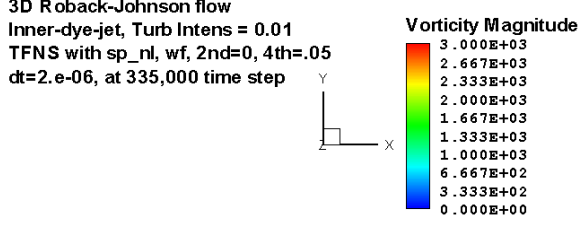
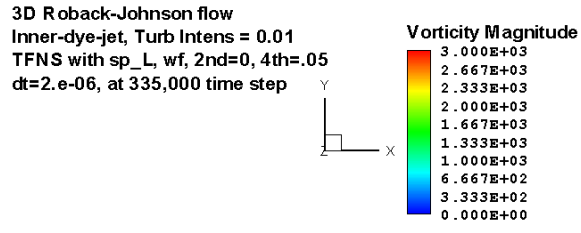


Figure 35.—Concluded.

3.3.7 Remarks

1. Concentration of the dye (issued from the inner jet) is well calculated at all streamwise locations.
 - a. Other flow quantities are also satisfactorily calculated: All velocity components (U , V , W) were in good agreement with the experimental data, except the azimuthal velocity decays faster towards downstream when compared with the experimental data. The center recirculation bubble matches its experimental counterpart.
 - b. Results from the TFNS simulations show significant improvements over the results from the RANS and URANS simulations. But they have not suggested a dramatic effect of the nonlinear subscale species flux model on either the concentration field or the flow field, i.e., the effect is positive, but small or very small.

3.4 Results of RANS Simulation Invoking the Scalar APDF Equation

In this section, the results of a steady RANS simulation invoking the scalar APDF equation are presented. The scalar APDF equation is solved by an Eulerian method. The main focus is to compare the performance of this hybrid approach with the performance of the pure RANS approach.

Figure 36 shows the contour plots of the axial velocity and the O_2 mass fraction of the dye in the X-Y center plane, and they are almost identical to their RANS counterparts presented in Section 3.1. Figure 37 and Figure 38 present the comparisons of the results from the hybrid RANS/APDF simulation and from the pure RANS simulation at downstream locations $x = 51$ and 102 mm. It can be seen that results from the two approaches are very close to each other.

3.4.1 Contour Plots of Variables in the X-Y Center Plane

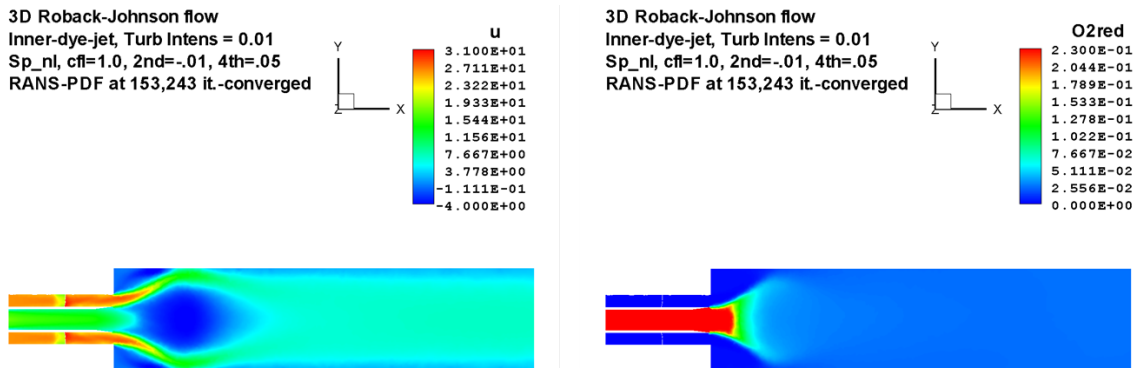


Figure 36.—Contours of axial velocity and O_2 mass fraction of the dye in X-Y center plane.

3.4.2 Radial Profiles of Concentration and Velocity Components at Downstream Locations

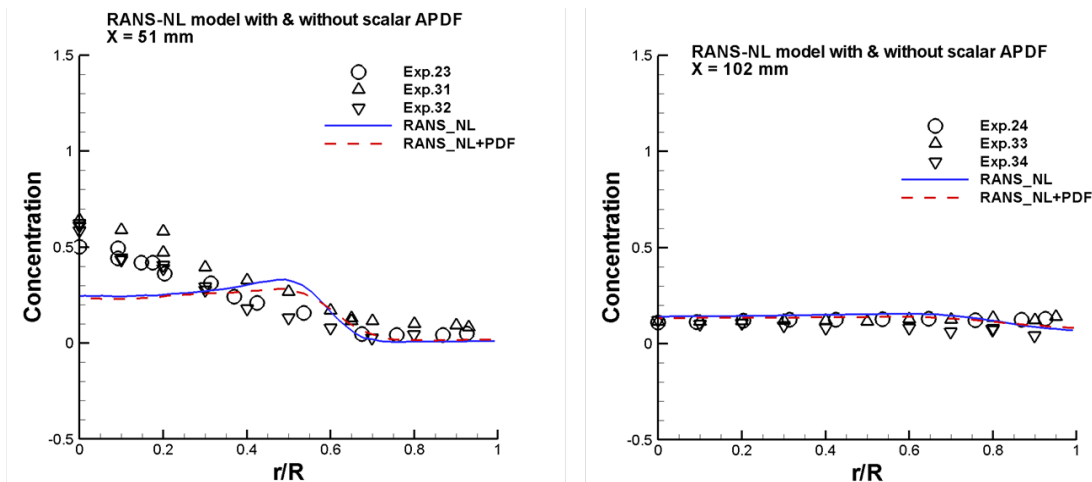


Figure 37.—Radial distributions of concentration at downstream locations.

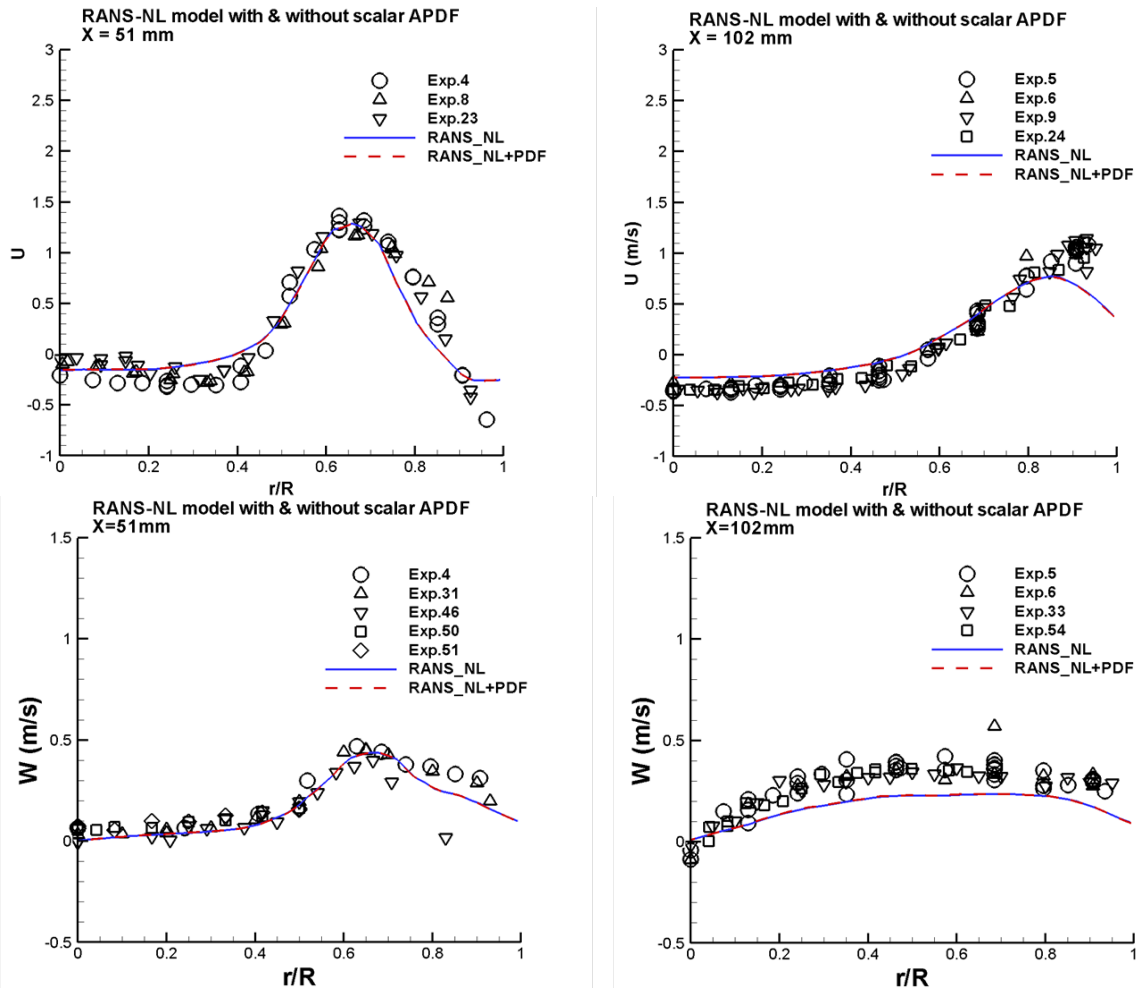


Figure 38.—Radial distributions of velocity components U , W at downstream locations.

3.5 Results of URANS Simulation Invoking the Scalar APDF Equation

In this section, the results of an unsteady RANS (URANS) simulation invoking the scalar APDF equation are presented. The scalar APDF equation is solved by an Eulerian method. The main focus is to compare the performance of this hybrid approach with the performance of the pure URANS approach.

Figure 39 shows the contour plots of the mean axial velocity and the mean O_2 mass fraction of the dye in the X-Y center plane, and they are almost identical to their URANS counterparts presented in Section 3.2. Figure 40, Figure 41 and Figure 42 present the comparisons of the results from the hybrid URANS/APDF simulation and from the pure URANS simulation along the centerline as well as at downstream locations $x = 25$ and 51 mm. It can be seen that results from the two approaches are very close to each other.

3.5.1 Contour Plots of Variables in the X-Y Center Plane

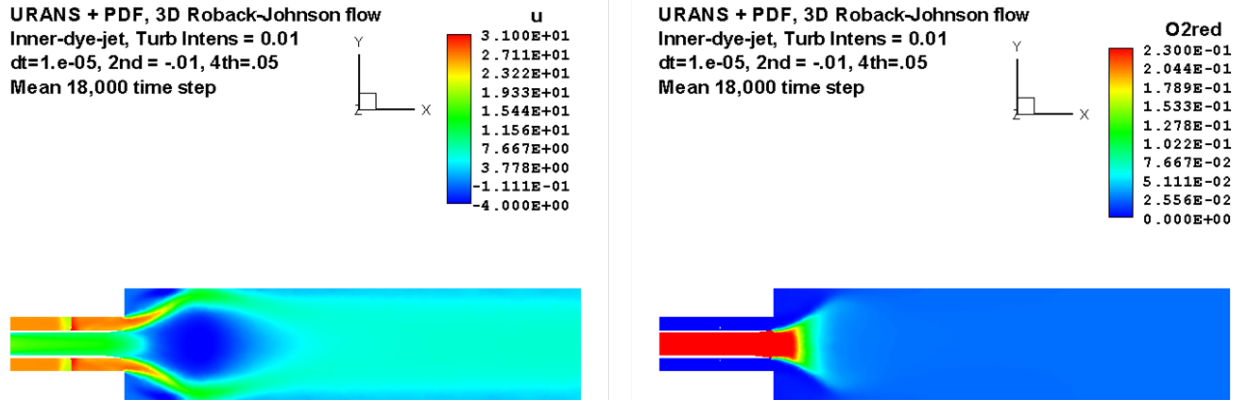


Figure 39.—Contours of axial velocity and O₂ mass fraction of the dye in X-Y center plane.

3.5.2 Centerline and Radial Profiles of Concentration

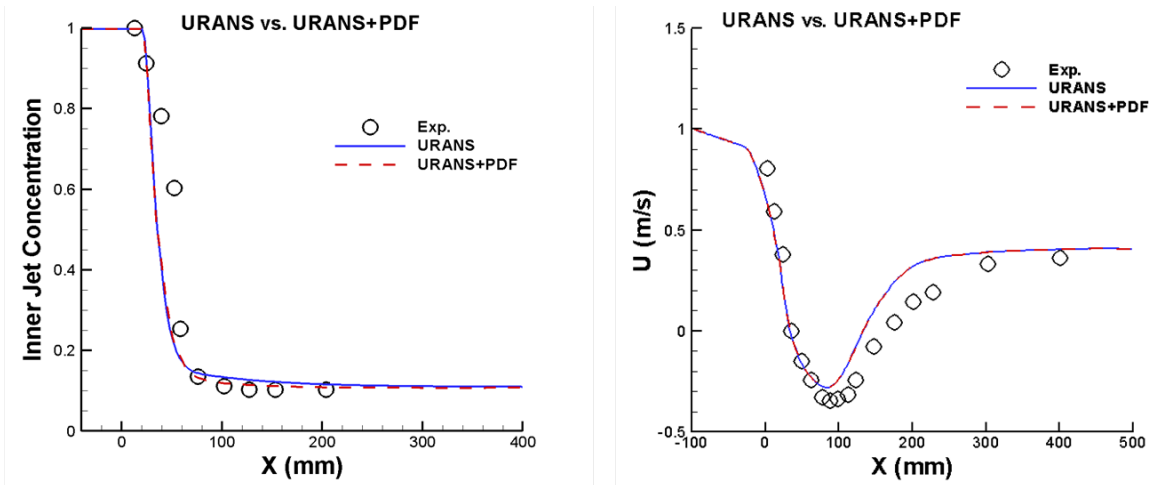


Figure 40.—Centerline distributions of concentration and axial velocity.

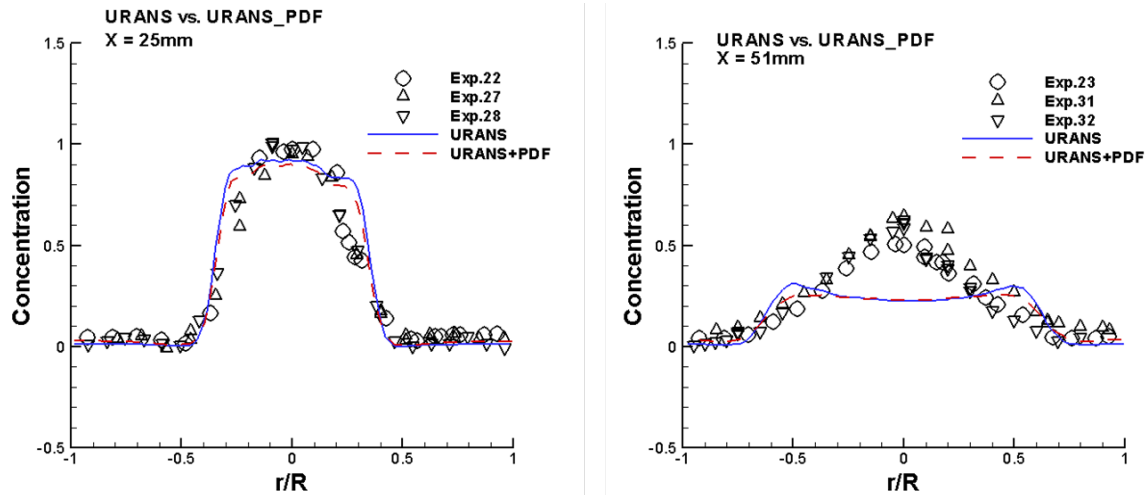


Figure 41.—Radial distributions of concentration at downstream locations.

3.5.3 Radial Profiles of Velocity Components at Downstream Locations

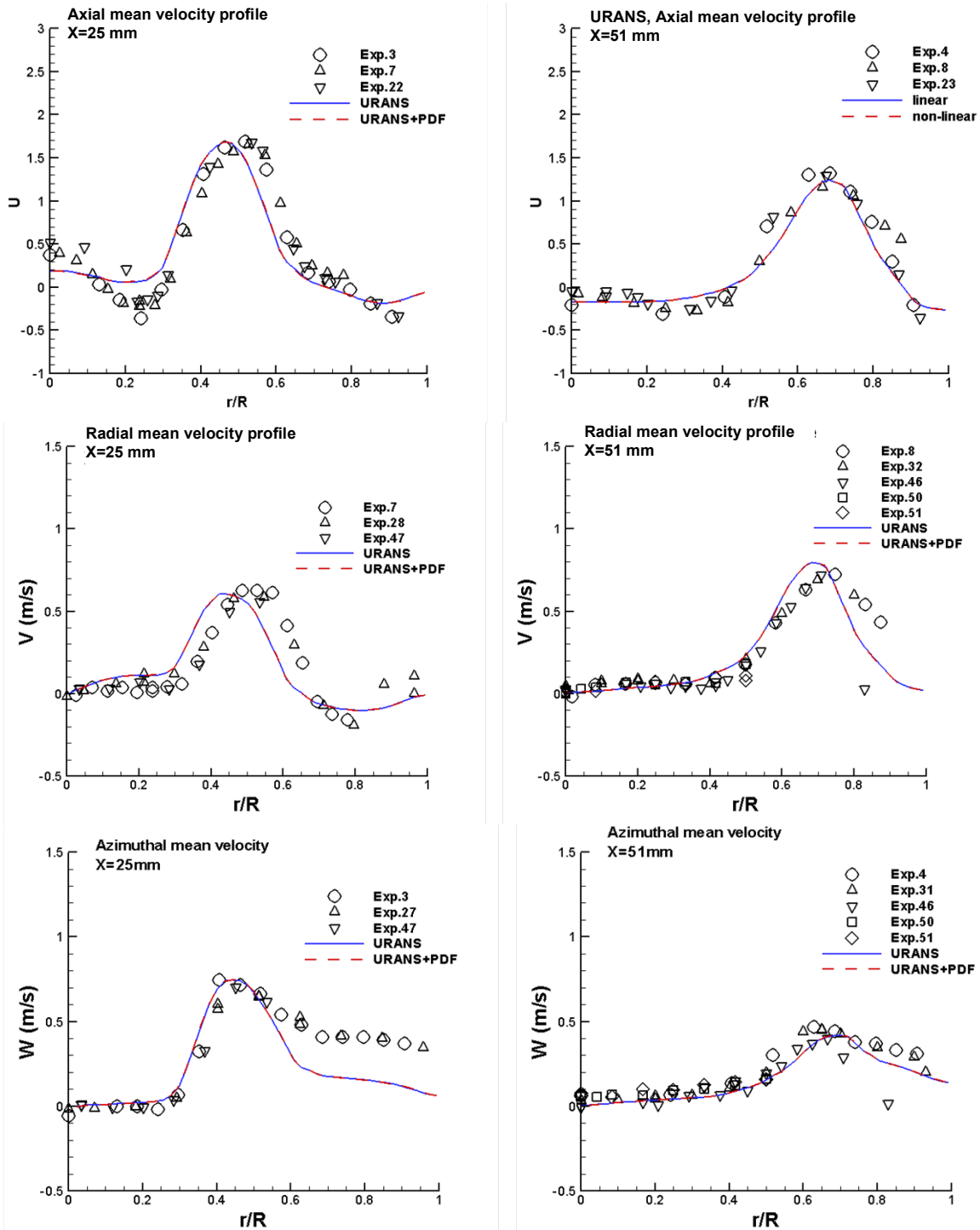


Figure 42.—Radial distributions of velocity components U , V , W at downstream locations.

3.6 Results of TFNS Simulation Invoking the Scalar DWFDF Equation

In this section, the results of a TFNS simulation invoking the scalar DWFDF equation are presented. The scalar DWFDF equation is solved by an Eulerian method. The main focus is to compare the performance of this hybrid approach with the performance of the pure TFNS approach.

Figure 43 shows the contour plots of the instantaneous axial velocity and the instantaneous O₂ mass fraction of the dye in the X-Y center plane. Figure 44, Figure 45 and Figure 46 present the comparisons of the results from the hybrid TFNS/DWFDF simulation and from the pure TFNS simulation along the centerline as well as at several downstream locations. It can be seen that results from the two approaches are very close to each other.

3.6.1 Contour Plots of Variables in the X-Y Center Plane

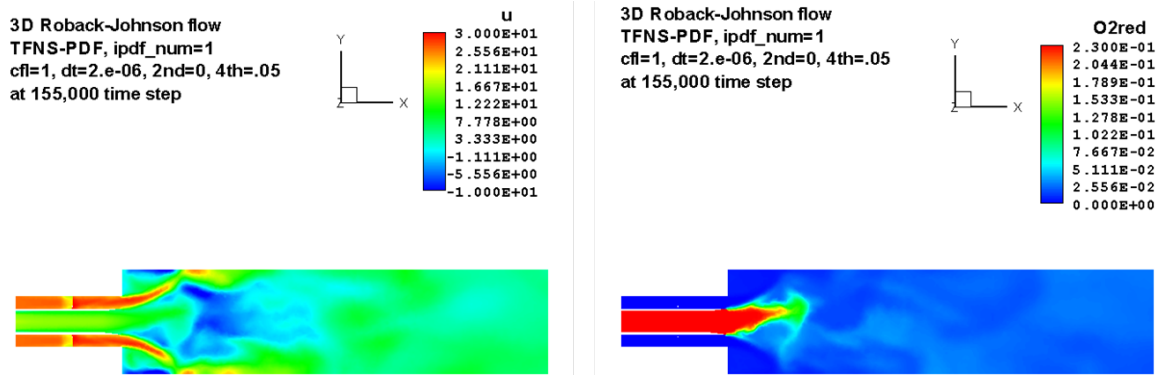


Figure 43.—Contours of instantaneous axial velocity and instantaneous O₂ mass fraction of the dye in X-Y center plane.

3.6.2 Centerline and Radial Profiles of Mean Concentration

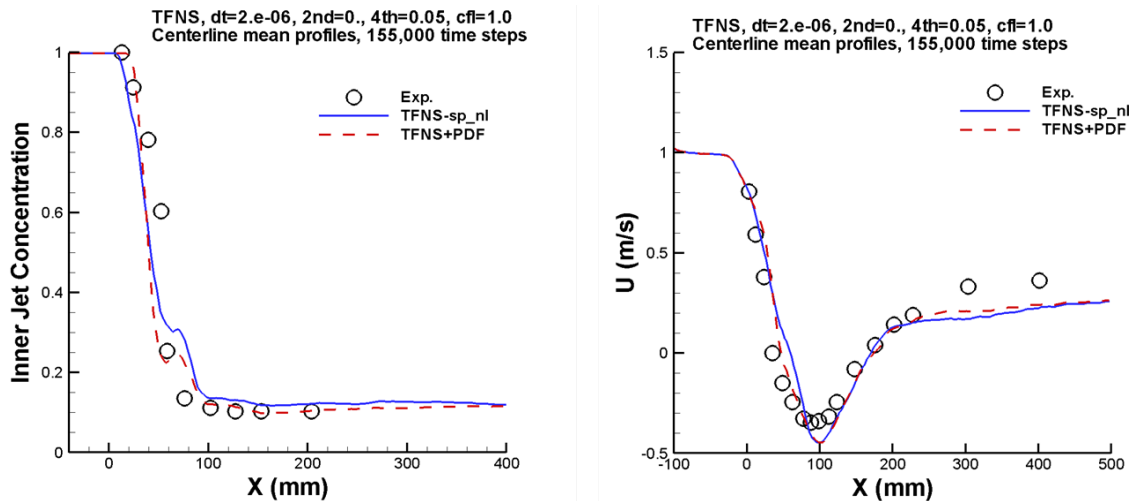


Figure 44.—Centerline distributions of concentration and axial velocity.

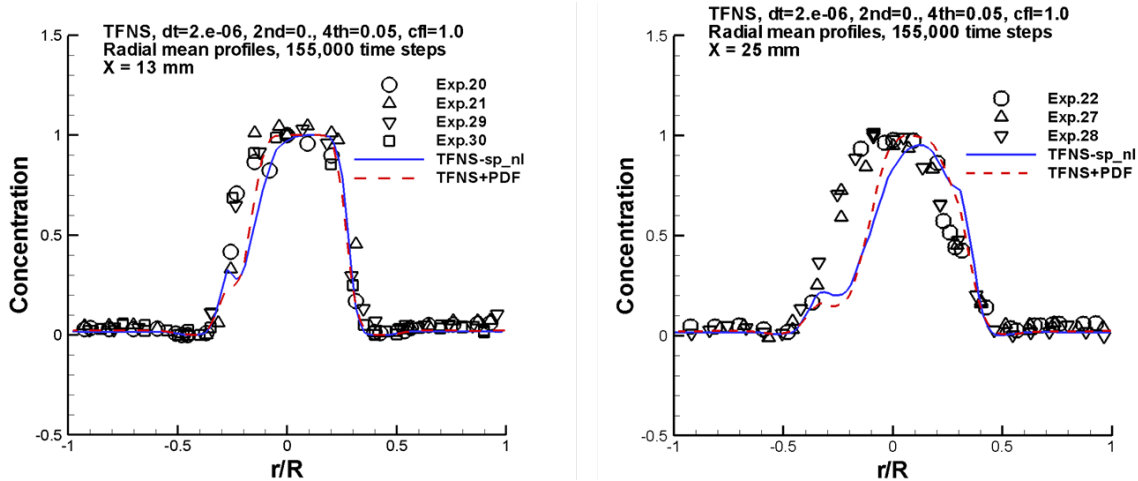


Figure 45.—Radial distributions of concentration at downstream locations.

3.6.3 Radial Profiles of Mean Velocity Components at Downstream Locations

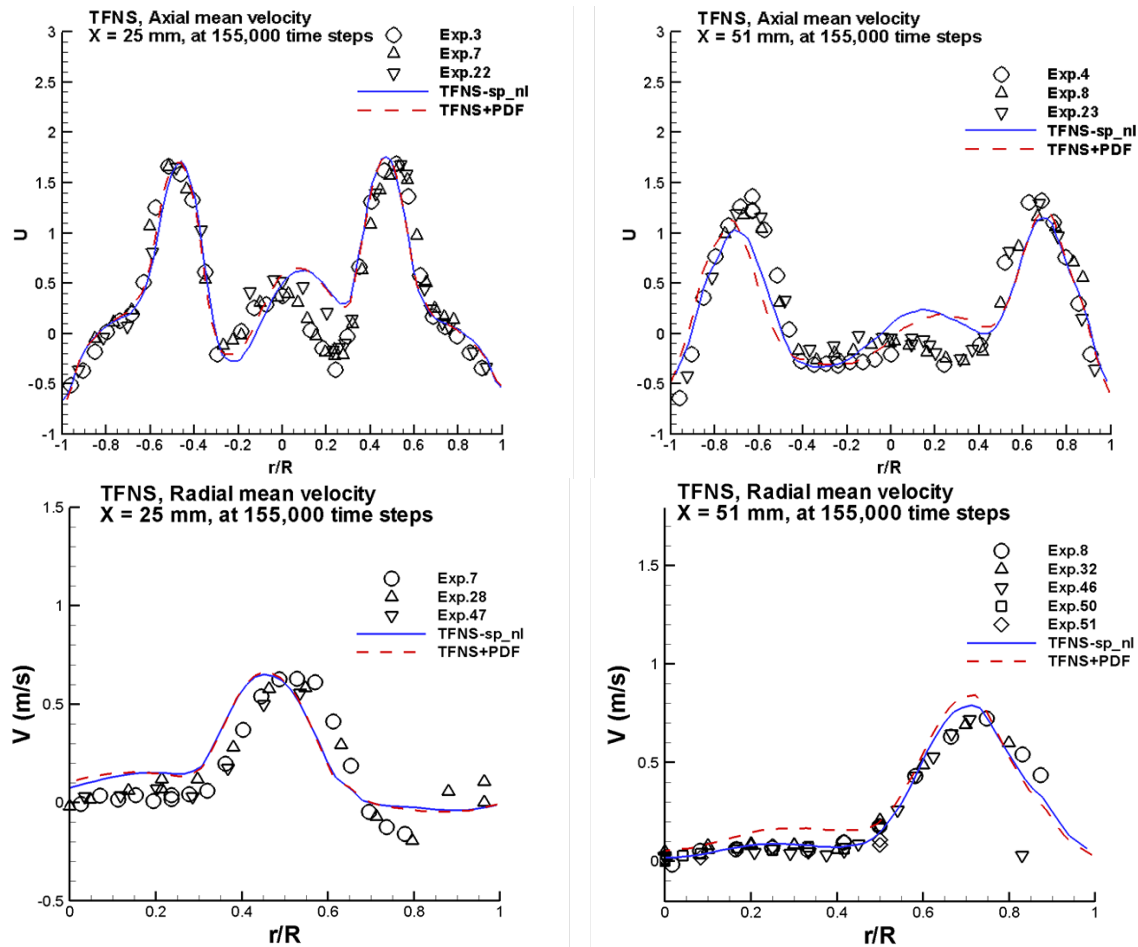


Figure 46.—Radial distributions of velocity components U , V , W at downstream locations.

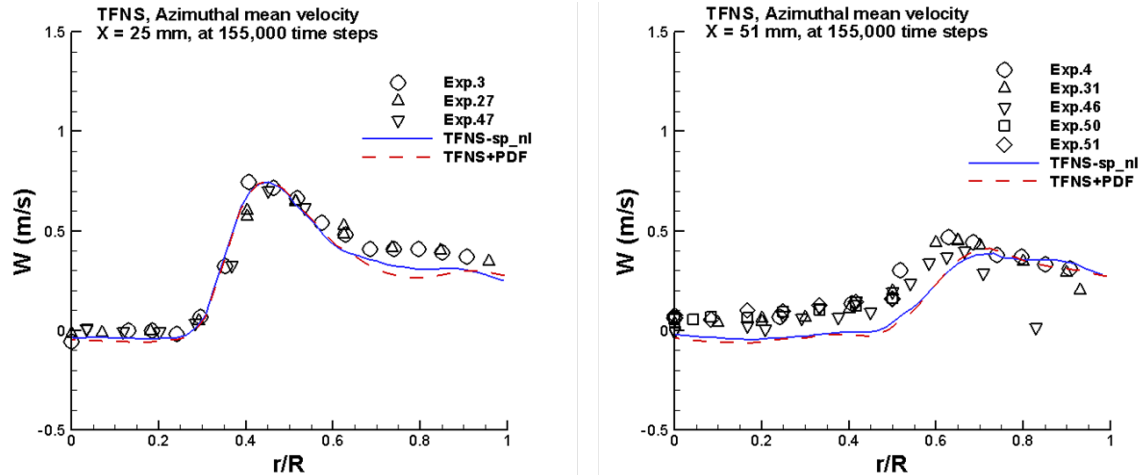


Figure 46.—Concluded.

4.0 Conclusion

Two groups of validations have been performed using the experiments of a confined swirling coaxial water jets flow. The first group focuses on the turbulent scalar flux model to explore the performance of the linear formulation versus the nonlinear formulation. Simulations conducted for this group include RANS, URANS and TFNS. The second group focuses on the hybrid approach to explore the performance of the newly introduced APDF and DWDFD equation and the Eulerian solver for this equation. Simulations conducted for this group include RANS/APDF, URANS/APDF and TFNS/DWDFD.

Regarding the scalar flux model, the linear and nonlinear model have the same behave in RANS and URANS simulation. Their respective results shown in various contour plots and profiles at different downstream locations are almost identical and in reasonable agreement with the experimental data. In the case of TFNS simulations, the differences of results from the linear and nonlinear models are small but noticeable. Furthermore, the TFNS results demonstrate significant improvements over their RANS and URANS counter parts, when compared with the experimental data.

Regarding the hybrid approach, the results of RANS/APDF, URANS/APDF and TFNS/DWDFD simulations show that they are very close to their respective RANS, URANS and TFNS counterpart. Our experiences so far have been that the hybrid approach appears to be more robust in the unsteady calculations and to converge faster, hence, using less computing time.

Appendix.—Simulations Using Standard $k - \epsilon$ Stress Model Versus Using Nonlinear Stress Model

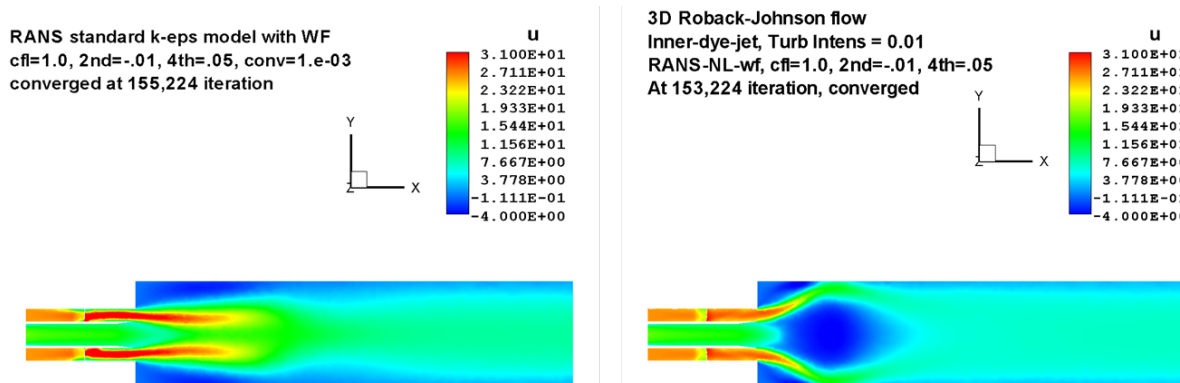
Here we present a set of RANS simulations for the purpose of comparing the performance of the standard $k - \epsilon$ model versus the performance of the nonlinear model.

1. RANS simulation with standard $k - \epsilon$ model:
 - a. Linear algebraic model for Reynolds stresses.
 - b. Linear scalar (i.e., heat and species) flux models.
 - c. Standard $k - \epsilon$ transport equations.
 - d. Constant $C_\mu = 0.09$.
 - e. Standard wall function.

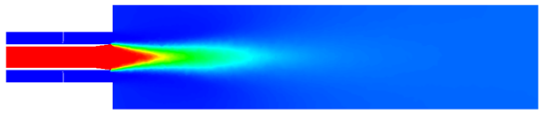
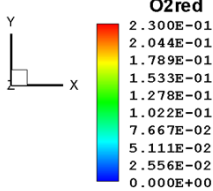
2. RANS simulation with nonlinear stress model:
 - a. Nonlinear (up to cubic powers) algebraic model for Reynolds stresses.
 - b. Nonlinear scalar (i.e., heat and species) flux models.
 - c. Standard $k - \epsilon$ transport equations.
 - d. Variable C_μ based on the realizability constraints.
 - e. Generalized wall function including the effects of wall pressure gradients.

3. Simulations start with the same initial condition, i.e., a RANS solution at the 120,000th iteration step, and use the same numerical parameters: $cfl = 1.0$, $2nd = -0.01$, $4th = 0.05$. Both simulations require about 40,000 iterations to reach the asymptotic steady state.

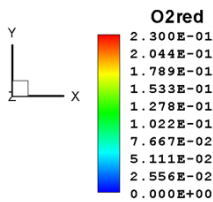
In the following, the presented results include the contour plots of axial velocity U , O_2 mass fraction of the dye, turbulent kinetic energy k and effective viscosity $\mu + \mu_T$, and also the centerline distribution of axial velocity U and concentration of the dye, the radial profiles of concentration at the downstream locations $x = 13, 25, 51$ and 102 mm, and the radial profiles of axial velocity U at the downstream locations $x = 51$ and 102 mm. It is quite clear that the standard $k - \epsilon$ model is not appropriate for calculating swirling coaxial jet flow, while the nonlinear stress model performs reasonably well for this type of flows.



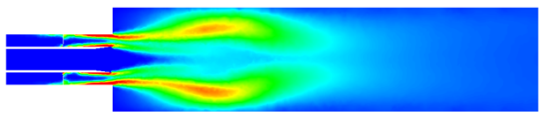
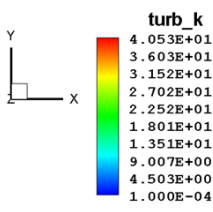
RANS standard k-eps model with WF
 cfl=1.0, 2nd=-.01, 4th=.05, conv=1.e-03
 converged at 155,224 iteration



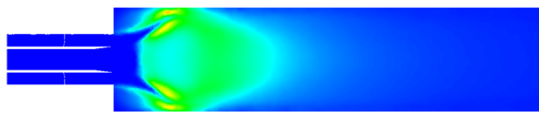
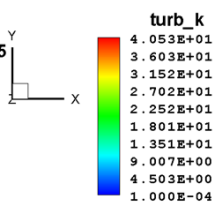
3D Roback-Johnson flow
 Inner-dye-jet, Turb Intens = 0.01
 RANS-NL-wf, cfl=1.0, 2nd=-.01, 4th=.05
 At 153,224 iteration, converged



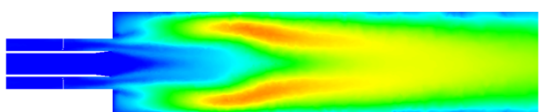
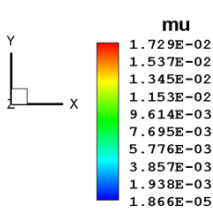
RANS standard k-eps model with WF
 cfl=1.0, 2nd=-.01, 4th=.05, conv=1.e-03
 converged at 155,224 iteration



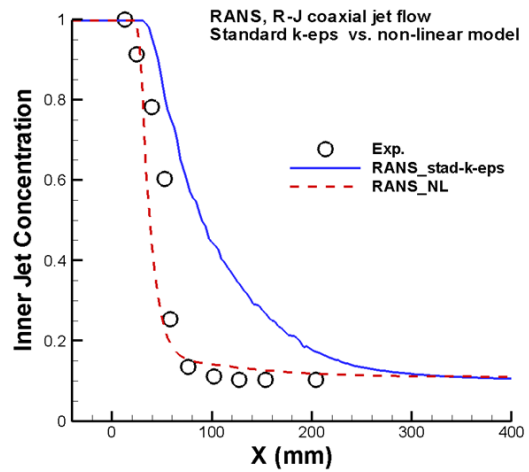
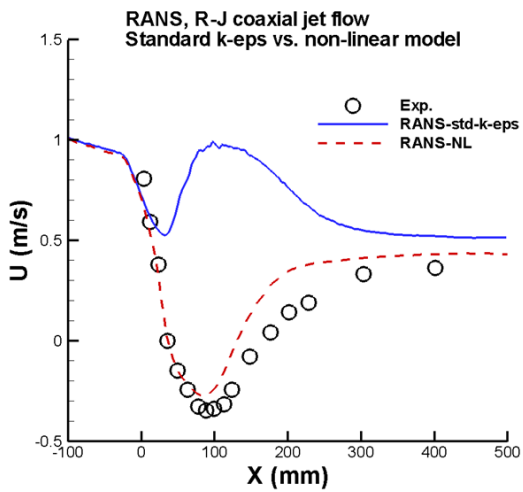
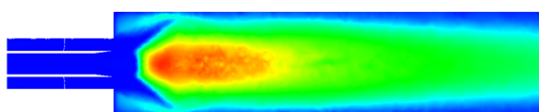
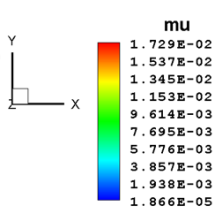
3D Roback-Johnson flow
 Inner-dye-jet, Turb Intens = 0.01
 RANS-NL-wf, cfl=1.0, 2nd=-.01, 4th=.05
 At 153,224 iteration, converged

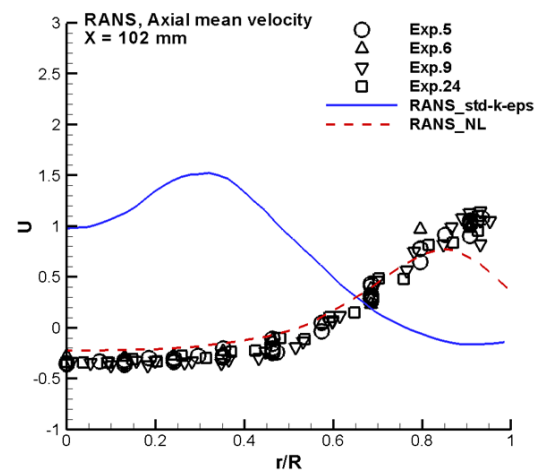
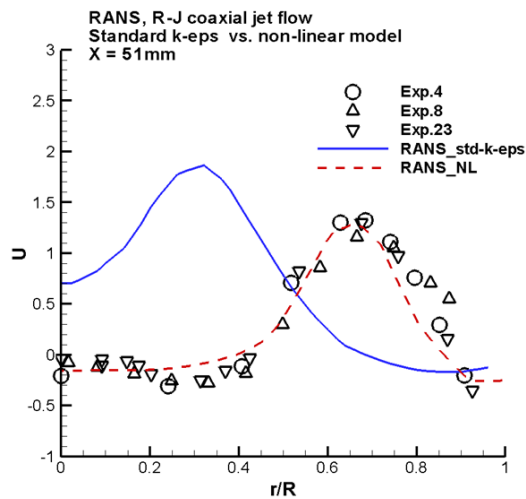
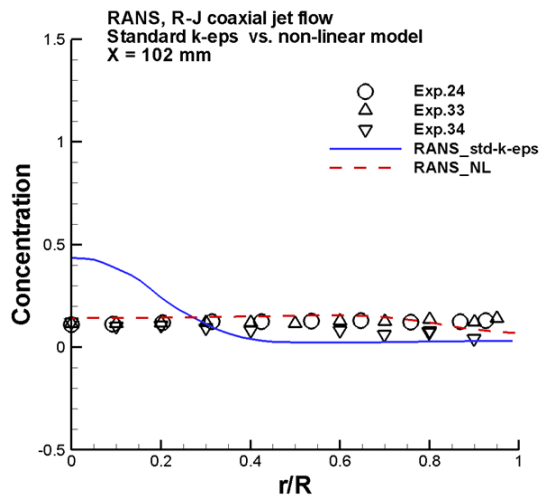
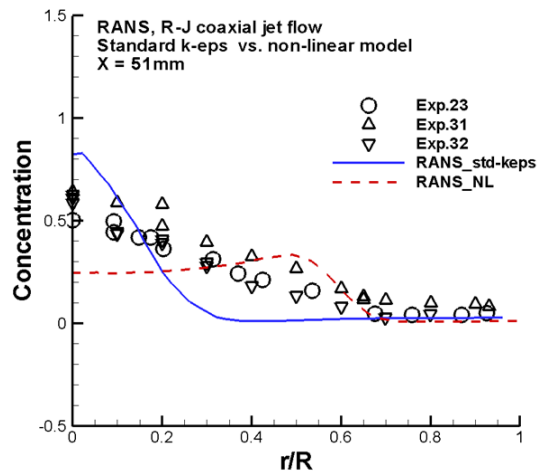
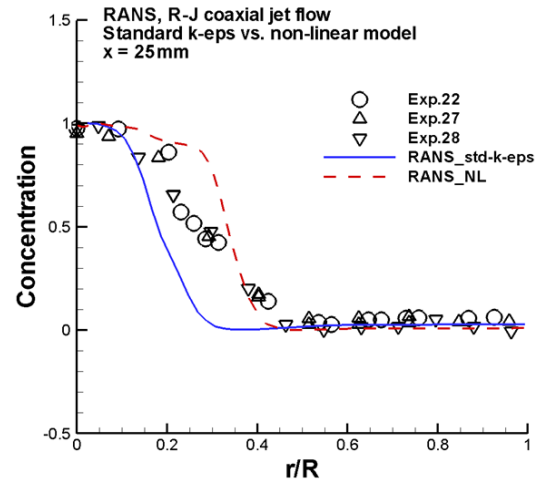
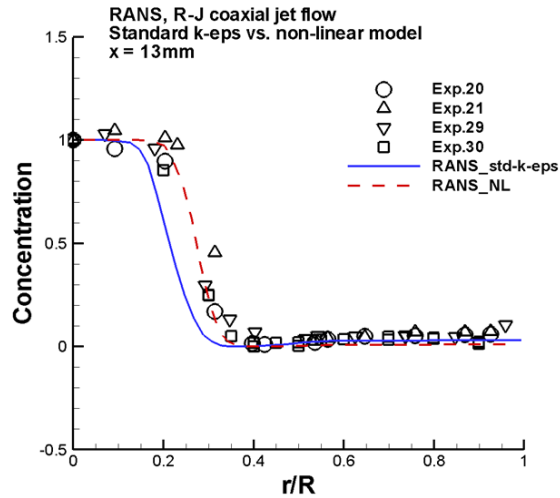


RANS standard k-eps model with WF
 cfl=1.0, 2nd=-.01, 4th=.05, conv=1.e-03
 converged at 155,224 iteration



3D Roback-Johnson flow
 Inner-dye-jet, Turb Intens = 0.01
 RANS-NL-wf, cfl=1.0, 2nd=-.01, 4th=.05
 At 153,224 iteration, converged





References

1. Liu, N.-S., "On the Comprehensive Modeling and Simulation of Combustion Systems," AIAA-2001-0805, January 2001.
2. Roback, R. and Johnson, B. V., "Mass and Momentum Turbulent Transport Experiments with Confined Swirling Coaxial Jets," NASA CR-168252, August 1983.
3. Shih, T.-H. and Liu, N.-S., "Ensemble Averaged Probability Density Function (APDF) Equations for Compressible Turbulent Reacting flows," NASA/TM-2012-217677, August, 2012.
4. Shih, T.-H. and Liu, N.-S., "Density Weighted FDF Equations for Simulations of Turbulent Reacting Flows," NASA/TM-2011-217012, May 2011.
5. Liu, N.-S., and Shih, T.-H., "Turbulence Modeling for Very Large-Eddy Simulation," AIAA Journal, Vol. 44, No. 4, 2006, pp. 687-697.
6. Shih, T.-H., and Liu, N.-S., "A non-linear Dynamic Subscale Model for Partially Resolved Numerical Simulation (PRNS)/Very Large Eddy Simulation (VLES) of Internal Non-Reacting Flows," NASA/TM-2010-216323, May 2010.
7. Raju, M.S., EUPDF-II: "An Eulerian Joint Scalar Monte Carlo PDF Module Users' Manual," NASA/CR-2004-213073.
8. Shih, T.-H., "Constitutive Relations and Realizability of Single-Point Turbulence Closures" Turbulence and Transition Modelling, Chapter 4., Edited by Hallback, M., Henningson, D.S., Johansson, A.V. and Alfredsson, P.H., Kluwer Academic Publishers, 1996.
9. Shih, T.-H., Zhu, J., Liou, W., Chen, K.-H., Liu, N.-S. and Lumley, J. L., " Modeling of Turbulent Swirling Flows," NASA/TM-1997-113112, 1997.
10. Shih, T.-H., "Some developments in computational modeling of turbulent flows," Fluid Dynamic Research 20 (1997) 67-96.
11. Ryder, R. C., "Application of the National Combustion Code Towards Unsteady Mixing and Combustion Modeling," AIAA-2000-0335, January 2000.

REPORT DOCUMENTATION PAGE			Form Approved OMB No. 0704-0188		
<p>The public reporting burden for this collection of information is estimated to average 1 hour per response, including the time for reviewing instructions, searching existing data sources, gathering and maintaining the data needed, and completing and reviewing the collection of information. Send comments regarding this burden estimate or any other aspect of this collection of information, including suggestions for reducing this burden, to Department of Defense, Washington Headquarters Services, Directorate for Information Operations and Reports (0704-0188), 1215 Jefferson Davis Highway, Suite 1204, Arlington, VA 22202-4302. Respondents should be aware that notwithstanding any other provision of law, no person shall be subject to any penalty for failing to comply with a collection of information if it does not display a currently valid OMB control number.</p> <p>PLEASE DO NOT RETURN YOUR FORM TO THE ABOVE ADDRESS.</p>					
1. REPORT DATE (DD-MM-YYYY) 01-08-2014		2. REPORT TYPE Technical Memorandum		3. DATES COVERED (From - To)	
4. TITLE AND SUBTITLE Simulations of Turbulent Momentum and Scalar Transport in Confined Swirling Coaxial Jets				5a. CONTRACT NUMBER	
				5b. GRANT NUMBER	
				5c. PROGRAM ELEMENT NUMBER	
6. AUTHOR(S) Shih, Tsan-Hsing; Liu, Nan-Suey				5d. PROJECT NUMBER	
				5e. TASK NUMBER	
				5f. WORK UNIT NUMBER WBS 794072.02.03.05.01	
7. PERFORMING ORGANIZATION NAME(S) AND ADDRESS(ES) National Aeronautics and Space Administration John H. Glenn Research Center at Lewis Field Cleveland, Ohio 44135-3191				8. PERFORMING ORGANIZATION REPORT NUMBER E-18930	
9. SPONSORING/MONITORING AGENCY NAME(S) AND ADDRESS(ES) National Aeronautics and Space Administration Washington, DC 20546-0001				10. SPONSORING/MONITOR'S ACRONYM(S) NASA	
				11. SPONSORING/MONITORING REPORT NUMBER NASA/TM-2014-218134	
12. DISTRIBUTION/AVAILABILITY STATEMENT Unclassified-Unlimited Subject Categories: 01 and 64 Available electronically at http://www.sti.nasa.gov This publication is available from the NASA Center for AeroSpace Information, 443-757-5802					
13. SUPPLEMENTARY NOTES					
14. ABSTRACT This paper presents the numerical simulations of confined three dimensional coaxial water jets. The objectives are to validate the newly proposed nonlinear turbulence models of momentum and scalar transport, and to evaluate the newly introduced scalar APDF and DWDFD equation along with its Eulerian implementation in the National Combustion Code (NCC). Simulations conducted include the steady RANS, the unsteady RANS (URANS), and the time-filtered Navier-Stokes (TFNS) with and without invoking the APDF or DWDFD equation. When the APDF or DWDFD equation is invoked, the simulations are of a hybrid nature, i.e., the transport equations of energy and species are replaced by the APDF or DWDFD equation. Results of simulations are compared with the available experimental data. Some positive impacts of the nonlinear turbulence models and the Eulerian scalar APDF and DWDFD approach are observed.					
15. SUBJECT TERMS Combustion CFD					
16. SECURITY CLASSIFICATION OF:			17. LIMITATION OF ABSTRACT	18. NUMBER OF PAGES	19a. NAME OF RESPONSIBLE PERSON
a. REPORT	b. ABSTRACT	c. THIS PAGE			STI Help Desk (email:help@sti.nasa.gov)
U	U	U	UU	60	19b. TELEPHONE NUMBER (include area code) 443-757-5802

